JOURNAL OF GUIDANCE, CONTROL, AND DYNAMICS
Vol. 31, No. 3, May–June 2008

Prediction of Icing Effects on the Coupled Dynamic Response of Light Airplanes

Amanda Lampton* and John Valasek†
Texas A&M University, College Station, Texas 77843-3141

DOI: 10.2514/1.31165

Most methods for the preliminary safety and performance evaluation of airplane dynamical response, stability characteristics, and climb performance in icing conditions require relatively sophisticated methods, based on detailed empirical data and existing flight data. This paper extends a pitch axis 3-degree-of-freedom methodology to the fully coupled, 6-degree-of-freedom case. It evaluates various levels of icing severity and addresses distributed icing with unequal ice distribution between wing halves on the coupled pitch, roll, and yaw responses. The important aspect of dynamic response sensitivity to pilot control input with the autopilot disabled is also highlighted. Using only basic mass properties, configuration, propulsion data, and known icing data from a similar configuration, icing effects are applied to the 6-degree-of-freedom dynamics of a nonreal-time simulation model of a different, but similar, light airplane. Results presented in the paper for a series of simulated climb maneuvers and cruise disturbances with equal or unequal ice levels between wing halves show that the methodology captures the basic effects of ice accretion on the coupled pitch, roll, and yaw responses and the sensitivity of the dynamic response to pilot control inputs.

NOMENCLATURE

A	=	plant matrix
B	=	control distribution matrix
C	=	output matrix
$C_{(A)}$	=	arbitrary stability and control derivative
$C_A(A)_{\text{iced}}$	=	arbitrary stability and control derivative with icing effects
C_D	=	airplane drag coefficient
C_L	=	airplane lift coefficient
C_l	=	airplane rolling moment coefficient
C_m	=	airplane pitching moment coefficient
C_n	=	airplane yawing moment coefficient
C_Y	=	airplane side-force coefficient
C_Z	=	stability Z-axis coefficient
$\bar{c}$	=	mean geometric chord
D	=	carry through matrix
d	=	distance along body X axis
f_{ice}	=	icing factor
g	=	gravitational acceleration
h	=	integration step size
I_{xx}	=	airplane moment of inertia about X axis
I_{xz}	=	airplane moment of inertia about XZ plane
I_{yy}	=	airplane moment of inertia about Y axis
I_{zz}	=	airplane moment of inertia about Z axis
i	=	index, imaginary component
j	=	imaginary component
k	=	coefficient icing factor constant
k'_{C_A}	=	coefficient icing factor constant with respect to a stability and control derivative
L	=	roll angular acceleration
M	=	pitch angular acceleration
N	=	yaw angular acceleration
P	=	aircraft body-axis roll rate
p	=	perturbed aircraft body-axis roll rate
$\dot{p}$	=	aircraft body-axis roll acceleration
Q	=	aircraft body-axis pitch rate
q	=	perturbed aircraft body-axis pitch rate
$\dot{q}$	=	aircraft body-axis pitch acceleration
$\bar{q}$	=	dynamic pressure
R	=	aircraft body-axis yaw rate
r	=	perturbed aircraft body-axis yaw rate
$\dot{r}$	=	aircraft body-axis yaw acceleration
S	=	wing area
t	=	time
U	=	aircraft velocity in the body-axis x direction
$\boldsymbol{U}$	=	control input vector
u	=	perturbed aircraft stability axis velocity in the x direction
$\dot{u}$	=	aircraft stability axis acceleration in the x direction
V	=	aircraft velocity in the body-axis y direction
W	=	aircraft velocity in the body-axis z direction
$\dot{w}$	=	aircraft body-axis acceleration in the z direction
X	=	linear acceleration in the body-axis x direction
$\boldsymbol{X}$	=	state vector
$\dot{\boldsymbol{X}}$	=	derivative of state vector
Y	=	linear acceleration in the body-axis y direction
$\boldsymbol{Y}$	=	output vector
Z	=	linear acceleration in the body-axis z direction
α	=	angle of attack
$\dot{\alpha}$	=	rate of change of angle of attack
β	=	sideslip angle
$\dot{\beta}$	=	rate of change of sideslip angle
Γ	=	discrete control distribution matrix
δ	=	control deflection angle
η_{ice}	=	icing severity factor
Θ_1	=	aircraft steady-state pitch attitude angle
θ	=	pitch attitude angle
$\dot{\theta}$	=	rate of change of pitch attitude angle
ξ	=	modal vector
τ	=	time constant
ν	=	eigenvector
Φ	=	discrete plant matrix
Φ_1	=	aircraft steady-state roll attitude angle
ϕ	=	roll attitude angle
$\dot{\phi}$	=	rate of change of roll attitude angle
Ψ_1	=	aircraft steady-state yaw attitude angle

Received 20 March 2007; revision received 19 November 2007; accepted for publication 20 November 2007.

*Graduate Research Assistant, Flight Simulation Laboratory, Aerospace Engineering Department; alampton@tamu.edu. Member AIAA.

†Associate Professor and Director, Flight Simulation Laboratory, Aerospace Engineering Department; valasek@tamu.edu. Associate Fellow AIAA.

ψ = yaw attitude angle
$\dot{\psi}$ = rate of change of yaw attitude angle
ω = frequency

Subscripts

0 = derivative with respect to zero angle of attack; initial condition
1 = steady-state; first mode
2 = second mode
3 = third mode
4 = fourth mode
5 = fifth mode
6 = sixth mode
7 = seventh mode
8 = eighth mode
a = aileron
d = Dutch roll mode
e = elevator
ice = ice accretion effect
iced = ice accretion effect
k = index for discretized model
m = modal
mgc = mean geometric chord
p = phugoid mode; derivative with respect to aircraft roll rate
q = derivative with respect to aircraft pitch rate
r = rudder; roll mode; derivative with respect to aircraft yaw rate
s = spiral mode
sp = short period mode
T_u = derivative with respect to change in speed due to thrust
T_α = derivative with respect to change in angle of attack due to thrust
u = derivative with respect to aircraft stability axis velocity in the x direction
α = derivative with respect to angle of attack
$\dot{\alpha}$ = derivative with respect to rate of change of angle of attack
β = derivative with respect to sideslip angle
$\dot{\beta}$ = derivative with respect to rate of change of sideslip angle
δ_a = derivative with respect to aileron deflection angle
δ_e = derivative with respect to elevator deflection angle
δ_r = derivative with respect to rudder deflection angle

Superscripts

T = transpose

I. Introduction

INCLEMENT weather accounted for an average of 19.6% of environment-related reported general aviation accidents annually from 1998 to 2000 according to the National Transportation Safety Board [1–3]. Of this annual percentage, icing conditions accounted for 2.9% of general aviation accidents in 1997, 2.4% in 1998, 3.6% in 1999, and 2.7% in 2000, for which 36.4, 55.6, 46.2, and 40.0% of those resulted in fatalities in 1997, 1998, 1999, and 2000, respectively [1–4]. Rime, glaze, and mixed ice along the leading edge of lifting surfaces all have detrimental effects on airplane performance. Although anti-icing devices such as de-icing boots and heating strips help, ice accretions can still build up and affect the airplane adversely by decreasing static lateral stability, especially in the case when the airplane does not develop ice accretions evenly between wing halves. Additionally, malfunctions of these anti-icing systems can result in ice buildup aft of the devices themselves, or ice buildup between the cycles of the de-icing systems. The type and severity of ice accretions is highly dependent on a number of factors. These include, but are not limited to, the following: velocity of the airplane, exposure time, atmospheric air temperature, liquid water content, and median volumetric diameter.

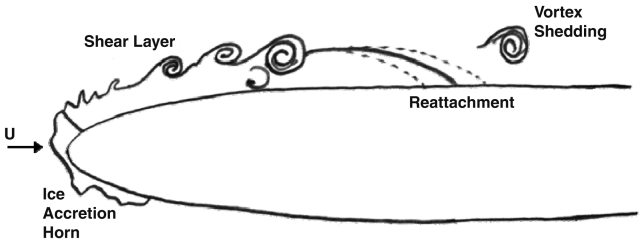

Fig. 1 Schematic of upper surface separation bubble aft of leading-edge ice accretion [5].

The danger of a longitudinal or lateral maneuver with ice accretions on the airplane lays in the susceptibility of the ice causing a separation bubble (Fig. 1) [5]. This phenomenon is usually caused by a horn of ice disrupting the flow of air over the airfoil and creating an adverse pressure gradient. This disruption forms a separation bubble that reattaches further downstream. However, increasing the deflection angle of the ailerons or elevator increases the relative angle of attack, thus pushing the reattachment point farther downstream and increasing the size of the separation bubble.

As the bubble increases in size, elevator, aileron, and rudder effectiveness decreases and full departure of the airplane becomes more likely. Ice accretions on the vertical tail can form a similar separation bubble phenomenon. The effect of full tail icing has been shown to decrease weathercock stability, C_{n_β}, as well as reduce rudder effectiveness [5]. Bragg et al. have developed an icing effects model applicable to any performance, stability, or control derivative affected by icing [6]. The model is characterized by a dependence on atmospheric conditions, the susceptibility of an airplane to icing, and a given derivative as seen in Eq. (1):

$$C_{(A)_{\text{iced}}} = (1 + \eta_{\text{ice}} k'_{C_A}) C_{(A)} \tag{1}$$

This model is still being refined, with many of the influencing factors still unknown [6]. The model was then integrated into a flight dynamics and control toolbox for MATLAB and Simulink, which produces results showing the possible changes of an airplane's stability derivatives over time with icing effects.[‡]

The practicality of using an autopilot during icing conditions has also been studied. Sharma et al. have designed a pitch angle hold autopilot that considers ice accretion severity when processing the commanded pitch attitude angle, the goal being to maintain the stability of the airplane [7]. The commanded value for the pitch attitude angle is then modified based on an envelope protection algorithm that references flight-test data of ice severity and wing stall angle of attack [7]. The purpose is to prevent the airplane from reaching the icing modified wing stall angle of attack, and pitch attitude response is investigated. Distributed levels and severities of icing between the wing and horizontal tail are not specifically addressed, and the iced airplane model and the autopilot are applicable only to the DeHavilland Twin Otter [7]. Additionally, the important aspect of sensitivity of airplane response to pilot command inputs in icing conditions with the autopilot disabled, which is the autopilot status recommended by the Federal Aviation Administration (FAA) in these conditions, is not addressed.

The area of forensic engineering is also concerned with the effect ice has on climb performance and aerodynamic degradation [8]. The research described in Sibilski et al. [8] concerns the dangerous reduction in the stall angle of attack and how climbing at high angles of attack could approach this reduced stall angle, causing an unexpected wing stall. The nonlinear simulation incorporating the effects of ice accretion was set up specifically for a jet trainer in an attempt to project the trajectory of a crash caused by ice accretion [8].

[‡]Data available online. See M. Rauw, "FDC 1.3 - A SIMULINK Toolbox for Flight Dynamics and Control Analysis," http://www.mathworks.com/matlabcentral/leexchange [retrieved 2007].

Reehorst et al. [9] employ Navier–Stokes analysis to test the flowfield and resulting lift and drag produced by a wing section with various ice shapes. The most significant finding is that 5 min ice accretions were found to produce severe lift and drag degradation.

Much other research in the area of the influence of ice regards airfoil aerodynamics. Lee and Bragg explore the changes in airfoil section lift, drag, and pitching moment with simulated ice shapes [10]. Intercycle ice accretions have a distinct effect on airfoil properties as described in Broeren et al. [11]. In this case, the build up of ice between pneumatic boot inflation and the possible ice ridge left just behind where the boot meets the skin of the airfoil is analyzed [11]. The resulting increase in drag, decrease in lift, and change in pitching moment is tabulated [11]. In general, the consensus appears to be that the aerodynamics of an airfoil is degraded by ice accretion such that lift decreases, drag increases, stall angle of attack is reduced, and pitching moment is degraded [8,10,12–17].

Efforts have been made to develop icing protection systems, especially Bragg et al. They propose a smart icing system based on the ability to sense the effect of ice on airplane performance, stability, and control [18]. The system would enhance the level of safety offered by current icing avoidance and protection concepts [18]. The Smart Icing System senses ice accretion through traditional icing sensors and uses modern system identification methods to estimate airplane performance and control changes [19]. Melody et al. [20] developed a method to monitor in-flight ice accretion effects using parameter identification. The authors state that parameter estimation must be timely and accurate. An H^{∞} method is found to indicate timely and accurate icing effects.

Airplane response due to pilot command inputs with the autopilot disengaged is a critical safety issue, because the FAA recommends that the autopilot must be disengaged during flight in known icing conditions. The danger lies in a pilot attempting to command an iced airplane in the same way as a non-iced airplane, because overly aggressive pilot command inputs (for the iced situation) can produce excessive climb rates that can lead to stall, overshoots and undershoots in commanded altitude, and excessive rolling and pitching moments. This is particularly critical for situations in which the pilot is not even aware that the airplane response and performance has been compromised by icing, and it has not been reported on in the open literature.

Lampton and Valasek [21] developed a simplified method for the prediction of icing effects and pilot command effects on the dynamic response, stability, and climb performance of light airplanes. Their method permits a rapid, first-cut prediction and analysis of the performance of icing effects using only basic, relatively easy to obtain or generate data as a precursor to a highly detailed analysis using sophisticated and costly modeling and analysis methods. It is equally applicable to either performance prediction or accident reconstruction and has been used for both. A feature of the method is the modeling and analysis of airplanes for which icing data does not exist or is not available in the open literature. This is done using known icing data obtained from either flight data or wind-tunnel data or both for airplanes of similar but different configurations, using appropriate scaling and modification. A linear time-invariant (LTI), 3-degree-of-freedom, state-space mathematical model of the longitudinal dynamics of a light airplane was derived and used for developing a nonreal-time simulation to evaluate distributed icing effects on stability and control characteristics. Sensitivity to pilot command inputs during icing conditions in terms of dynamic response were investigated, with the autopilot disengaged as per the FAA recommendation. The approach and results were all limited to the pitch axis only and therefore did not account for the lateral/directional dynamics or the coupled response between the three axes.

Lampton and Valasek [22] also investigated unequal icing distributions between the right and left half of the wing, which can result when flying in icing conditions with a crosswind. The component buildup method was used to implement icing effects on the wing alone and on the horizontal tail alone, and various unequal distributions of combined wing and horizontal tail icing, as well as ice accretion on only one half of the wing, were implemented. An LTI state-space mathematical model of the lateral/directional dynamics of a light airplane was derived and used for developing a nonreal-time simulation to evaluate distributed icing effects and various levels of ice accretion on the stability, control, and dynamic response characteristics. The scope of this work was limited to the roll and yaw axes and, therefore, did not account for the longitudinal dynamics or the coupled response between the three axes.

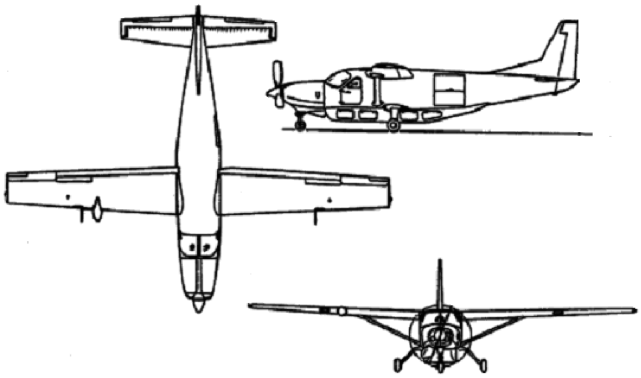

Fig. 2 Cessna 208B Super Cargomaster external characteristics.

The unique contribution of this paper to the literature is the extension of the 3-degree-of-freedom asymmetrically distributed icing methodologies of Lampton and Valasek [21,22] to the previously uninvestigated fully coupled 6-degree-of-freedom longitudinal and lateral/directional asymmetrically distributed icing case. The paper addresses the modeling of kinematic and force coupling, asymmetric icing, and various icing severity levels between the wing, the horizontal tail, one half of a wing, and the full airplane. An LTI state-space, coupled, 6-degree-of-freedom mathematical model is derived and used for developing a nonreal-time simulation. Validation of the simulation model is conducted using several basic maneuvers, and verification is conducted by comparing flight-test data for the same airplane as the simulation. Metrics consisting of the rate of climb, overshoots and undershoots of commanded altitude, and airplane rates that indicate roll off or departure tendencies are used to evaluate a variety of time-varying pilot inputs, such as singlets, doublets, and ramps, during icing conditions. Sensitivity to pilot command inputs during icing conditions, in terms of dynamic response with the autopilot disengaged as per the FAA recommendation, is also investigated.

The paper is organized as follows. First, a nonparametric coupled longitudinal and lateral/directional linear model of a Cessna 208B Super Cargomaster (Fig. 2 and Table 1) is derived, for which stability and control derivatives are calculated using the DATCOM and Advanced Aircraft Analysis (AAA) computer program [23]. Verification of the model is accomplished by comparing simulation data to published flight-test data. To ensure the fidelity of the model, a modal analysis was conducted to examine the characteristics of the flight modes. In addition, a controllability analysis was conducted to check that the system was indeed linearly independent and controllable. Next, the stability derivatives calculated for each flight condition of interest are used to construct multiple LTI state-space

Table 1 Change in stability and control derivatives because of icing [6]

Parameter	Value
b, ft	52.16
d_{mgc}, ft	11.80
i_W, deg	2.62
I_{xx}	8640.0
I_{xz}, slug $*$ ft$^{(2)}$	555.7
I_{yy}, slug $*$ ft$^{(2)}$	14375.0
I_{zz}, slug $*$ ft$^{(2)}$	21189.9
S, ft$^{(2)}$	279.40
S_H, ft$^{(2)}$	70.04
Weight, lb	8402.0
η_H	0.945

models. Various levels of ice accretion severity are then added to the clean airplane simulation based on icing data gathered by the NASA John H. Glenn Research Center at Lewis Field on the DeHavilland Twin Otter [6] A series of simulation examples are presented for either climb maneuvers or perturbations in cruise with varying amounts of ice accretion between wing halves. Finally, a summary and conclusions are presented.

II. State-Space Model Representation

The system analyzed in this paper is an LTI system of the combined longitudinal and lateral/directional dynamics represented in the stability axis.

Figure 3 shows the body-axis systems for reference. The time invariance of the model is assumed because the parameters in the model do not change quickly for the relatively slow maneuvers examined here. Consider first the linear time-invariant state-space model of perturbations about the steady-state or trim condition:

$$\dot{\boldsymbol{X}} = A\boldsymbol{X} + B\boldsymbol{U} \qquad \boldsymbol{Y} = C\boldsymbol{X} + D\boldsymbol{U} \tag{2}$$

where $\boldsymbol{X} \in \mathbb{R}^{n\times 1}$ is a state vector, $A \in \mathbb{R}^{n\times n}$ is a plant matrix, $\boldsymbol{U} \in \mathbb{R}^{m\times 1}$ is an input vector, $B \in \mathbb{R}^{n\times m}$ is a control distribution matrix, $\boldsymbol{Y} \in \mathbb{R}^{r\times 1}$ is an output vector, and $C \in \mathbb{R}^{r\times n}$ and $D \in \mathbb{R}^{r\times m}$ are matrices that determine the elements of the output vector.

A. Coupled Longitudinal and Lateral/Directional State-Space Model

Considering the longitudinal and lateral/directional dynamics of an airplane, the perturbed equations of motion of this coupled system can be represented as Taylor series expansions in the stability axes with respect to a steady, level, 1-g-trimmed flight condition, such that $P_1 = Q_1 = R_1 = V_1 = W_1 = 0, \Theta_1 = \text{constant}$, and $\Phi_1 = \text{constant}$. Coupling between the longitudinal and lateral/directional axes is accounted for through the kinematics and the major force coupling derivatives X_β and Z_ϕ. These are the only two coupling derivatives used, because all of the remaining coupling derivatives have been found to be negligible by comparison [24]. The affine in the control, coupled, linear time-invariant perturbation equations are

$$\dot{u} = -g\theta\cos\Theta_1 + (X_{T_u} + X_u)u + X_\alpha\alpha + X_q q + X_{\delta_e}\delta_e + X_{\delta_T}\delta_T + X_{\dot{\alpha}}\dot{\alpha} + X_\beta$$

$$\dot{\alpha} = \frac{\dot{w}}{U_1} = (-g\theta\sin\Theta_1\cos\Phi_1 + Z_u u + Z_\alpha\alpha + Z_q q + U_1 q + Z_{\delta_e}\delta_e + Z_{\delta_T}\delta_T + Z_{\dot{\alpha}}\dot{\alpha} + Z_\phi - g\phi\cos\Theta_1\sin\Phi_1)/U_1$$

$$\dot{q} = (M_{T_u} + M_u)u + (M_{T_\alpha} + M_\alpha)\alpha + M_q q + M_{\delta_e}\delta_e + M_{\delta_T}\delta_T + M_{\dot{\alpha}}\dot{\alpha}$$

$$\dot{\theta} = q\cos\Phi_1 - r\sin\Phi_1$$

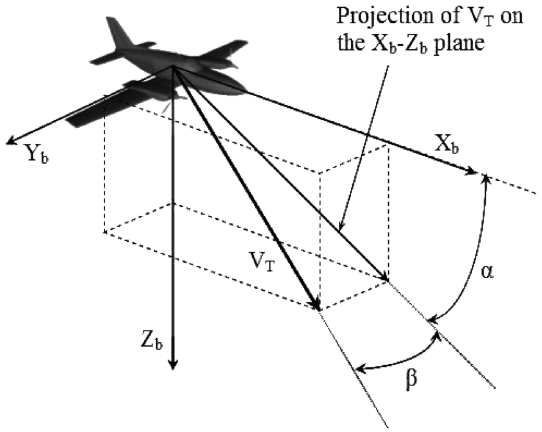

Fig. 3 Body-axis systems and aerodynamic angles.

$$\dot{\beta} = (Y_p p + g\phi\cos\Theta_1\cos\Phi_1 + g\theta\sin\Theta_1\sin\Phi_1 + Y_\beta\beta + (Y_r - U_1)r + Y_{\delta_A}\delta_A + Y_{\delta_R}\delta_R)/U_1$$

$$\dot{p} = L_\beta\beta + L_p p + L_r r + L_{\delta_A}\delta_A + L_{\delta_R}\delta_R + \frac{I_{xz}}{I_{xx}}\dot{r}$$

$$\dot{r} = N_\beta\beta + N_p p + N_r r + N_{\delta_A}\delta_A + N_{\delta_R}\delta_R + \frac{I_{xz}}{I_{zz}}\dot{p}$$

$$\dot{\phi} = p + r\cos\Phi_1\tan\Theta_1 + q\sin\Phi_1\tan\Theta_1$$

$$\dot{\psi} = r\cos\Phi_1\sec\Theta_1 + q\sin\Phi_1\sec\Theta_1 \tag{3}$$

Premultiplying by the mass matrix E

$$E = \begin{bmatrix} 1 & -X_{\dot{\alpha}} & 0 & 0 & 0 & 0 & 0 & 0 & 0 \\ 0 & 1-\frac{Z_{\dot{\alpha}}}{U_1} & 0 & 0 & 0 & 0 & 0 & 0 & 0 \\ 0 & -M_{\dot{\alpha}} & 1 & 0 & 0 & 0 & 0 & 0 & 0 \\ 0 & 0 & 0 & 1 & 0 & 0 & 0 & 0 & 0 \\ 0 & 0 & 0 & 0 & 1 & 0 & 0 & 0 & 0 \\ 0 & 0 & 0 & 0 & 0 & 1 & -\frac{I_{xz}}{I_{xx}} & 0 & 0 \\ 0 & 0 & 0 & 0 & 0 & -\frac{I_{xz}}{I_{zz}} & 1 & 0 & 0 \\ 0 & 0 & 0 & 0 & 0 & 0 & 0 & 1 & 0 \\ 0 & 0 & 0 & 0 & 0 & 0 & 0 & 0 & 1 \end{bmatrix} \tag{4}$$

produces

$$E\dot{\boldsymbol{X}} = A\boldsymbol{X} + B\boldsymbol{U} \Rightarrow \dot{\boldsymbol{X}} = E^{-1}A\boldsymbol{X} + E^{-1}B\boldsymbol{U} \tag{5}$$

where the state coefficient or plant matrix $A \in \mathbb{R}^{n\times n}$ is now transformed into

$$E^{-1}A = \begin{bmatrix} X'_u & X'_\alpha & X'_q & X'_\theta & X'_\beta & 0 & 0 & 0 & 0 \\ Z'_u & Z'_\alpha & Z'_q & Z'_\theta & 0 & 0 & 0 & Z'_\phi & 0 \\ M'_u & M'_\alpha & M'_q & M'_\theta & 0 & 0 & 0 & 0 & 0 \\ 0 & 0 & \cos\Phi_1 & 0 & 0 & 0 & -\sin\Phi_1 & 0 & 0 \\ 0 & 0 & 0 & \frac{Y_\theta}{U_1} & \frac{Y_\beta}{U_1} & \frac{Y_p}{U_1} & \left(\frac{Y_r}{U_1} - 1\right) & \frac{g\cos\Theta_1}{U_1} & 0 \\ 0 & 0 & 0 & 0 & L'_\beta & L'_p & L'_r & 0 & 0 \\ 0 & 0 & 0 & 0 & N'_\beta & N'_p & N'_r & 0 & 0 \\ 0 & 0 & \sin\Phi_1\tan\Theta_1 & 0 & 0 & 1 & \cos\Phi_1\tan\Theta_1 & 0 & 0 \\ 0 & 0 & \sin\Phi_1\sec\Theta_1 & 0 & 0 & 0 & \cos\Phi_1\sec\Theta_1 & 0 & 0 \end{bmatrix} \tag{6}$$

in which the primed quantities result from collecting the $\dot{\alpha}$, $\dot{p}$, and $\dot{r}$ in the lift, roll rate, and yaw rate equations, respectively, and eliminating them from the other equations. The corresponding control distribution matrix with collected terms is

$$E^{-1}B = \begin{bmatrix} X'_{\delta_e} & X'_{\delta_T} & 0 & 0 \\ Z'_{\delta_e} & Z'_{\delta_T} & 0 & 0 \\ M'_{\delta_e} & M'_{\delta_T} & 0 & 0 \\ 0 & 0 & 0 & 0 \\ 0 & 0 & \frac{Y_{\delta_A}}{U_1} & \frac{Y_{\delta_R}}{U_1} \\ 0 & 0 & L'_{\delta_A} & L'_{\delta_R} \\ 0 & 0 & N'_{\delta_A} & N'_{\delta_R} \\ 0 & 0 & 0 & 0 \\ 0 & 0 & 0 & 0 \end{bmatrix} \tag{7}$$

where the primes result for the same reason already provided. The state and control vectors are represented by

$$\boldsymbol{X} = [u \;\; \alpha \;\; q \;\; \theta \;\; \beta \;\; p \;\; r \;\; \phi \;\; \psi]^T \tag{8}$$

$$\boldsymbol{U} = [\delta_e \;\; \delta_T \;\; \delta_a \;\; \delta_r]^T \tag{9}$$

Assembling Eqs. (6–9) results in the following state-space model

$$\begin{bmatrix} \dot{u} \\ \dot{\alpha} \\ \dot{q} \\ \dot{\theta} \\ \dot{\beta} \\ \dot{p} \\ \dot{r} \\ \dot{\phi} \\ \dot{\psi} \end{bmatrix} = \begin{bmatrix} X'_u & X'_\alpha & X'_q & X'_\theta & X'_\beta & 0 & 0 & 0 & 0 \\ Z'_u & Z'_\alpha & Z'_q & Z'_\theta & 0 & 0 & 0 & Z'_\phi & 0 \\ M'_u & M'_\alpha & M'_q & M'_\theta & 0 & 0 & 0 & 0 & 0 \\ 0 & 0 & \cos\Phi_1 & 0 & 0 & 0 & -\sin\Phi_1 & 0 & 0 \\ 0 & 0 & 0 & \frac{Y_\theta}{U_1} & \frac{Y_\beta}{U_1} & \frac{Y_p}{U_1} & \left(\frac{Y_r}{U_1} - 1\right) & \frac{g\cos\Theta_1}{U_1} & 0 \\ 0 & 0 & 0 & 0 & L'_\beta & L'_p & L'_r & 0 & 0 \\ 0 & 0 & 0 & 0 & N'_\beta & N'_p & N'_r & 0 & 0 \\ 0 & 0 & \sin\Phi_1 \tan\Theta_1 & 0 & 0 & 1 & \cos\Phi_1 \tan\Theta_1 & 0 & 0 \\ 0 & 0 & \sin\Phi_1 \sec\Theta_1 & 0 & 0 & 0 & \cos\Phi_1 \sec\Theta_1 & 0 & 0 \end{bmatrix} \begin{bmatrix} u \\ \alpha \\ q \\ \theta \\ \beta \\ p \\ r \\ \phi \\ \psi \end{bmatrix} + + \begin{bmatrix} X'_{\delta_e} & X'_{\delta_T} & 0 & 0 \\ Z'_{\delta_e} & Z'_{\delta_T} & 0 & 0 \\ M'_{\delta_e} & M'_{\delta_T} & 0 & 0 \\ 0 & 0 & 0 & 0 \\ 0 & 0 & \frac{Y_{\delta_A}}{U_1} & \frac{Y_{\delta_R}}{U_1} \\ 0 & 0 & L'_{\delta_A} & L'_{\delta_R} \\ 0 & 0 & N'_{\delta_A} & N'_{\delta_R} \\ 0 & 0 & 0 & 0 \\ 0 & 0 & 0 & 0 \end{bmatrix} \begin{bmatrix} \delta_e \\ \delta_T \\ \delta_a \\ \delta_r \end{bmatrix} \tag{10}$$

The elements of Eqs. (6) and (7) are determined from nondimensional stability and control derivatives extracted from AAA for a DATCOM model of the Cessna 208B developed using the maintenance manual for the airplane [25] and verified by flight-test data as shown in Sec. V for the longitudinal and lateral/directional dynamics. AAA is a software code based on the U.S. Air Force Data Compendium (DATCOM). Major assumptions made in the development of the DATCOM model were 1) the exact location of the transition point from laminar to turbulent flow on the lifting surfaces, 2) the drag increment due to gaps between lifting and control surfaces, 3) steady flow, and 4) the linear model is accurate up to angular displacements of 15 deg and velocity perturbations of up to 100 ft/ sec. A universal location of 14% of the chord of the lifting surface is used as the transition point from laminar to turbulent flow. For the drag increment, a value of 0.00036 is used. Coupled linear models of the Cessna 208B composed of the stability and control derivatives are provided in the Appendix.

B. Dynamic Characteristics

The detailed modal analysis in Lampton and Valasek [22,26] is summarized here. The longitudinal dynamics consist of the two standard modes, short period and phugoid, and the lateral/directional dynamics consist of the three standard modes, Dutch roll, roll, and spiral, all of which are stable for the flight condition considered.

Short period mode:

$$\lambda_{1,2} = -1.49 \pm 2.54j \qquad \omega_{\text{sp}} = 2.94 \text{ rad/s} \qquad \zeta_{\text{sp}} = 0.51 \tag{11}$$

Phugoid mode:

$$\lambda_{3,4} = -0.013 \pm 0.19\text{j} \qquad \omega_{\text{p}} = 0.2 \text{ rad/s} \qquad \zeta_{\text{p}} = 0.065 \tag{12}$$

Dutch roll mode:

$$\lambda_{5,6} = -1.49 \pm 2.54\text{j} \qquad \omega_{\text{d}} = 1.76 \text{ rad/s} \qquad \zeta_{\text{d}} = 0.21 \tag{13}$$

Roll mode:

$$\lambda_7 = -4.84 \qquad \tau_{\text{r}} = 0.21 \text{ s} \tag{14}$$

Spiral mode:

$$\lambda_8 = -0.016 \qquad \tau_{\text{s}} = 63.68 \text{ s} \tag{15}$$

A modal analysis was conducted to indicate contributions of each state and, in particular, each control to the various modes. For the Cessna 208B, the elevator is most effective in controlling the pitch attitude angle and, to a lesser extent, the angle of attack. The sideslip angle and the yaw angle are most affected by the ailerons and rudder, whereas the roll rate is only significantly affected by the ailerons. The yaw rate is affected to a lesser extent by the rudder. In terms of modes, the short period mode is made up primarily of the angle of attack and, to a lesser extent, the pitch rate. The phugoid mode is mainly composed of the pitch attitude angle and, to a lesser extent, the angle of attack and pitch rate. The Dutch roll mode is composed primarily of the yaw rate and, to a lesser extent, the roll attitude angle. The roll mode is composed of the sideslip and roll rate, whereas the spiral mode is composed mainly of the roll attitude angle and yaw rate. The composition of these five modes indicates the existence of the standard short period, phugoid, Dutch roll, roll, and spiral modes. A controllability analysis using the controllability grammian verifies that the system is controllable.

III. Simulation Development

Consistent with the scope of this work, which is to determine degradation due to ice accretions for several parameters via numerical simulation, the aforementioned continuous-time LTI model must be discretized. This discrete-time LTI system is defined as

$$\boldsymbol{X}_{k+1} = \Phi \boldsymbol{X}_k + \Gamma \boldsymbol{U}_k \qquad \boldsymbol{Y}_k = \boldsymbol{C}\boldsymbol{X}_k + \boldsymbol{D}\boldsymbol{U}_k \tag{16}$$

where $\Phi \in \mathbb{R}^{n\times n}$ and $\Gamma \in \mathbb{R}^{n\times m}$ are the state transition matrix and discrete control distribution matrix, respectively, and are dependent on $A \in \mathbb{R}^{n\times n}$, $B \in \mathbb{R}^{n\times m}$, and h, the time step of the discrete-time

model. Φ and Γ of the discrete model are related to their continuous model counterparts, A and B, by the following equations:

$$\Phi(h) = e^{Ah} \tag{17}$$

$$\Gamma = \left(\int_0^h e^{A\tau}\,\mathrm{d}\tau\right)B \tag{18}$$

The simulation is coded using MATLAB 7.1. By loading values determined from AAA for a given flight condition into the LTI state-space model in MATLAB, the discretized model can be determined using commands imbedded in the program. This is done for both a clean airplane and an iced airplane.

IV. Modeling and Incorporation of Icing Effects

The extent to which each stability and control derivative is affected by ice accretions is based on previous studies, in particular those concerning the flight dynamics of a DeHavilland Twin Otter [6,27]. The Twin Otter data were used because there is more icing data available of the type needed for this research than for any other airplane reported in the open literature. In general, the effectiveness of C_L, C_m, C_D, C_{L_α}, C_{m_α}, C_{D_α}, C_{L_q}, C_{m_q}, $C_{L_{\delta_e}}$, and $C_{m_{\delta_e}}$ for the longitudinal axis and C_{Y_β}, $C_{Y_{\delta_r}}$, C_{l_β}, C_{l_p}, $C_{l_{\delta_a}}$, $C_{l_{\delta_r}}$, C_{n_β}, C_{n_r}, and $C_{n_{\delta_r}}$ for the lateral/directional axes has been observed to degrade between 5 and 35%. As ice builds up on the leading edge of the wing, horizontal tail, and vertical tail, the carefully engineered surfaces are compromised, thus they produce less lift. Also, the ice accretion may develop horns that protrude into the airflow as well as increase the surface roughness, leading to an increase in drag. These changes in lift and drag contribute to changes in pitching, rolling, and yawing moments, especially in the event that ice only accretes on one half of the wing. The exact amount of degradation, whether it is an increase in drag, decrease in lift, or a change in pitching moment, side-force, rolling moment, or yawing moment, depends on both the airplane configuration and the particular derivative in question.

The percentage of degradation for each derivative of an evenly iced airplane is imbedded within the MATLAB program that dimensionalizes the values calculated by AAA. Each of these dimensionalized counterparts of the derivatives is multiplied by an icing factor, f_{ice}, causing the derivative in question to become less stable. For example, the modification for C_{l_β} is

$$L_{\beta_{\text{iced}}} = \frac{\bar{q}Sb(1 + f_{\text{ice}})C_{l_\beta}}{I_{xx}} \tag{19}$$

such that static stability is reduced as C_{l_β} decreases. In this case, an f_{ice} value of -0.10 is a degradation factor, meaning that C_{l_β} becomes less stable by 10% based on data from the DeHavilland Twin Otter [6]. For the numerical examples, these degradation factors are assumed to be the worst-case scenario for icing on the Cessna 208B.

Equation (19) generalizes the terms first presented in Eq. (1). For the purposes of this research, f_{ice} represents the term $\eta_{\text{ice}}k'_{C_A}$. The actual parameterization of the terms η_{ice} and k'_{C_A} is beyond the scope of this paper, but is being addressed by other researchers. Instead, f_{ice} for each pertinent derivative is calculated from flight-test data of the DeHavilland Twin Otter in both clean and icing conditions, as detailed in Bragg et al. [6]. Because comprehensive icing data is not readily available for the Cessna 208B, applying icing data obtained from the DeHavilland Twin Otter does not fully represent what actually occurs in icing conditions. However, the simulated dynamic responses and performance are consistent with the limited scope and objectives of this research. Values of f_{ice} are presented in Table 2.

To analyze how the flight dynamics and performance change with ice accretion severity, additional factors are included in the calculation of the iced derivatives to represent various levels of severity. For example, the nominal f_{ice} degradation factor for C_{l_β} is -0.10, as already stated. For a totally iced condition, the worst case for the Cessna 208B is f_{ice} multiplied by 1.0. It is assumed that the 1.0 is implicit in Eq. (19). Similarly, if only mild icing is of interest, then f_{ice} may only be multiplied by 0.2, as shown in the following equation:

$$L_{\beta_{\text{iced}}} = \frac{\bar{q}Sb(1 + 0.2 * f_{\text{ice}})C_{l_\beta}}{I_{xx}} \tag{20}$$

For the particular example shown, $0.2f_{\text{ice}} = 0.2(-0.10) = -0.02$, which means that for "mild" ice C_{l_β} becomes less stable by 2%. This additional severity factor allows for increased versatility in examining the possible effects that icing has on the flight dynamics and performance of the airplane in question.

Table 2 Change in stability and control derivatives because of icing [6]

Derivative	Clean value	f_{ice}
$-C_{L_0}$	0.26	0
$(-C_{L_\alpha} - C_{D_1})$	−4.53	−0.10
$-C_{L_q}$	10.27	−0.012
$-C_{L_{\delta_e}}$	0.54	−0.095
C_{m_0}	0.10	0
C_{m_α}	−0.78	−0.099
C_{m_q}	−28.95	−0.035
$C_{m_{\delta_e}}$	−1.61	−0.10
C_{Y_β}	−1.04	−0.20
$C_{Y_{\delta_r}}$	0.23	−0.08
C_{l_β}	−0.10	−0.10
C_{l_p}	−0.59	−0.10
$C_{l_{\delta_a}}$	0.15	−0.10
$C_{l_{\delta_r}}$	0.02	−0.08
C_{n_β}	0.10	−0.20
C_{n_r}	−0.20	−0.061
$C_{n_{\delta_a}}$	−0.01	−0.083

A. Distributed Icing Effects

Predicting the extent and severity of ice accretion before encountering icing conditions can be difficult due to its dependence on the configuration of the airplane and numerous atmospheric conditions; an airplane may be easily affected by even the smallest amount of ice or it may be able to stay in flight without any adverse effects with very severe icing. In addition, an airplane does not necessarily have to accumulate ice evenly between lifting surfaces or between wing halves. Some airplanes tend to have a wing icing problem only, others a horizontal tail icing problem, and still others do in fact accumulate ice fairly evenly between lifting surfaces. It is assumed here that the effects of distributed icing (different levels of ice on the wing and horizontal tail) appear as changes in the lift force and drag force of a given lifting surface, such as a wing or a horizontal tail. Before adding the icing effect to the wing, tail, or wing half, an analysis is performed to determine the relative distribution of lift and drag between the wing fuselage and the horizontal tail.

If ice is added to only the right half of the wing, the method of applying icing factors to derivatives as described previously no longer applies. In this case, differences in lift and drag between the clean left wing and iced right wing will be used to determine the induced rolling and yawing moments due to ice and integrated into the state-space model described in previous sections.

This analysis is performed using trim values at 15,000 ft. Although a complete treatment of the propwash effect is beyond the scope of the simplified approaches used in this work, Eq. 8.41 of Roskam [28] is used to account for the propeller slipstream effect on the dynamic pressure at the horizontal tail. Starting with the relation for the total airplane lift coefficient and solving for the lift coefficient of the horizontal tail,

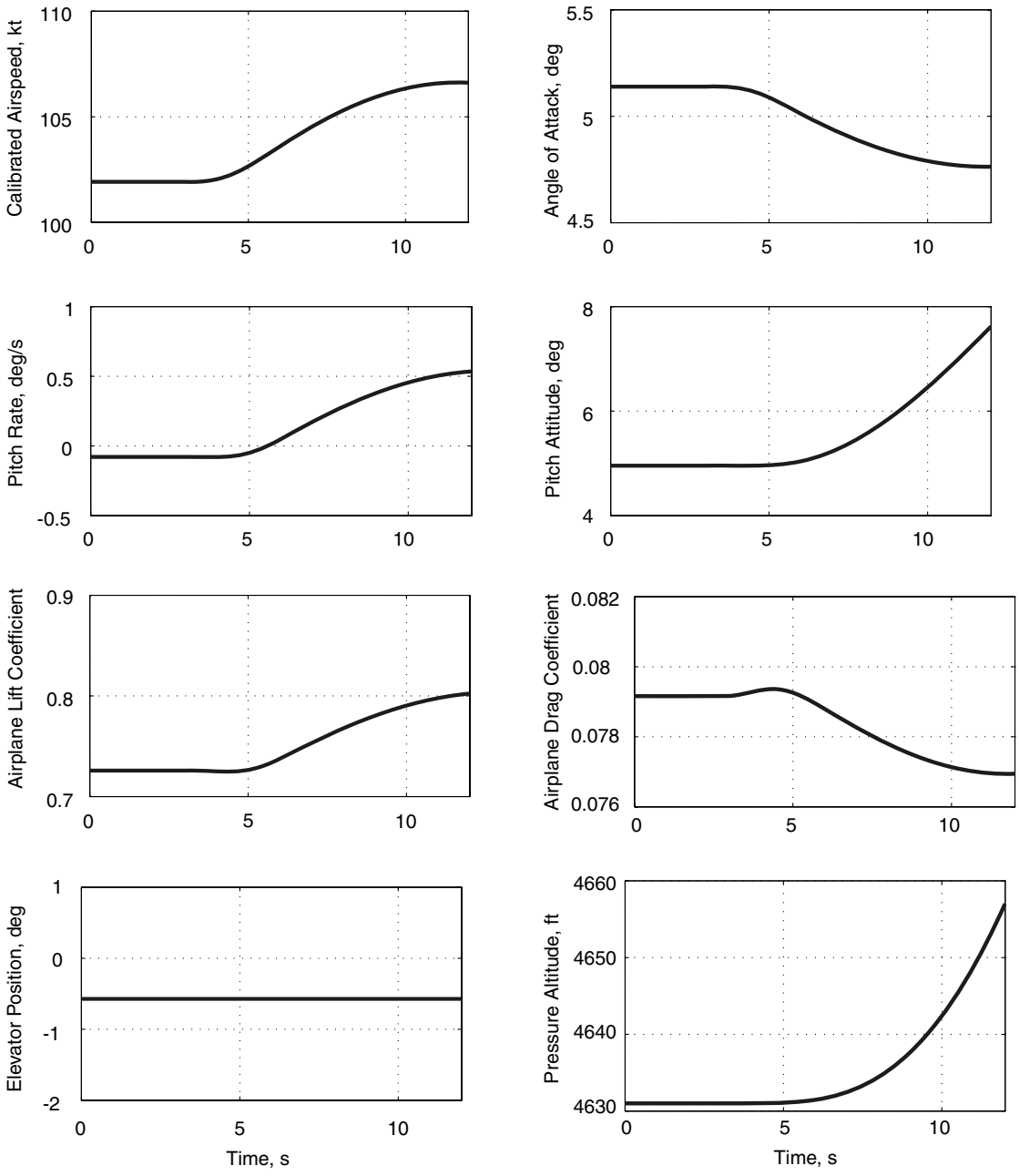

Fig. 4 Level acceleration responses.

$$C_L \bar{q} S = C_{L_{\mathrm{WF}}} \bar{q} S + C_{L_H} \bar{q}_H S_H$$

$$C_{L_H} = \frac{C_L \bar{q} S - C_{L_{\mathrm{WF}}} \bar{q} S}{\bar{q}_H S_H} = \frac{\bar{q}}{\bar{q}_H} \frac{S}{S_H} (C_L - C_{L_{\mathrm{WF}}}) \tag{21}$$

$$= \frac{1}{\eta} \frac{S}{S_H} (C_L - C_{L_{\mathrm{WF}}}) = \frac{1}{0.945} \left(\frac{279.4}{70.04} \right) (0.377 - 0.359) = 0.073$$

To determine the lift coefficient of the wing–fuselage combination,

$$C_{L_{\mathrm{WF}}} = C_{L_{o_{\mathrm{WF}}}} + C_{L_{\alpha_{\mathrm{WF}}}} \alpha_W = C_{L_{o_{\mathrm{WF}}}} + C_{L_{\alpha_{\mathrm{WF}}}} (\alpha + i_W)$$

$$= 0.034 + 4.779(1.285 + 2.62) \frac{1}{57.3} = 0.034 + 0.3257$$

$$= 0.359 \tag{22}$$

Finally, the lift distribution between the horizontal tail and wing is determined using the ratio of Eqs. (21) and (22) to be

Table 3 Level acceleration validation maneuver flight conditions and trim conditions

Altitude, ft	True airspeed, kt	Dynamic pressure, lbs/ft^2	Weight, lb	Center of gravity, $\bar{c}$	α_1, deg	δ_{e_1}, deg
4631	101.9	30.1	7591	0.289	5.14	1.22

Table 4 Longitudinal verification maneuver flight conditions and trim conditions

Altitude, ft	True airspeed, kt	Dynamic pressure, lbs/ft^2	Weight, lb	Center of gravity, $\bar{c}$	α_1, deg	δ_{e_1}, deg
4631	101.9	30.1	7591	0.291	5.14	−0.57

$$\frac{C_{L_H}}{C_{L_{\mathrm{WF}}}} = \frac{0.073}{0.359} = 0.203 \qquad C_{L_H} = 0.203 C_{L_{\mathrm{WF}}} \tag{23}$$

Thus, the horizontal tail generates approximately 20% of the lift that the wing fuselage generates. Although drag data was not available, drag data for a similar airplane configuration were used to provide a sanity check on the zero lift drag coefficients. Using $C_{D_{0_W}} = 0.37 C_{D_0}$ and $C_{D_{0_H}} = 0.07 C_{D_0}$,

$$C_{D_{0_H}} = \frac{0.07}{0.34} = 0.21 C_{D_{0_W}} \tag{24}$$

which confirms that the horizontal tail drag is also in the approximate proportion of 20% of the drag of the wing. Based on the values obtained in Eqs. (23) and (24) , a 20% proportion is selected for the asymmetric icing condition. This proportion means that, rather than calculating the dimensionalized derivative for the whole airplane and applying f_{ice} as in Eq. (19), each derivative is split into two components that are then added together using the component buildup method. This split allows for a separate icing factor to be applied to the lift and drag contribution of the wing and the lift and drag contribution of the horizontal tail.

B. Asymmetric Icing Effects

The next challenge is to calculate the change in lift and drag if ice accumulates on the right half of the wing only and the resulting rolling and yawing moments. Such a phenomenon is possible should the de-icing mechanism on only one wing half fail. The right half of the wing is chosen because the resulting differences in lift and drag between the two wing halves result in positive lateral/directional moments. The component buildup method is used employing the aforementioned lifting surface asymmetry. The percent due solely to the wing is then halved for both the lift and drag equations. Icing

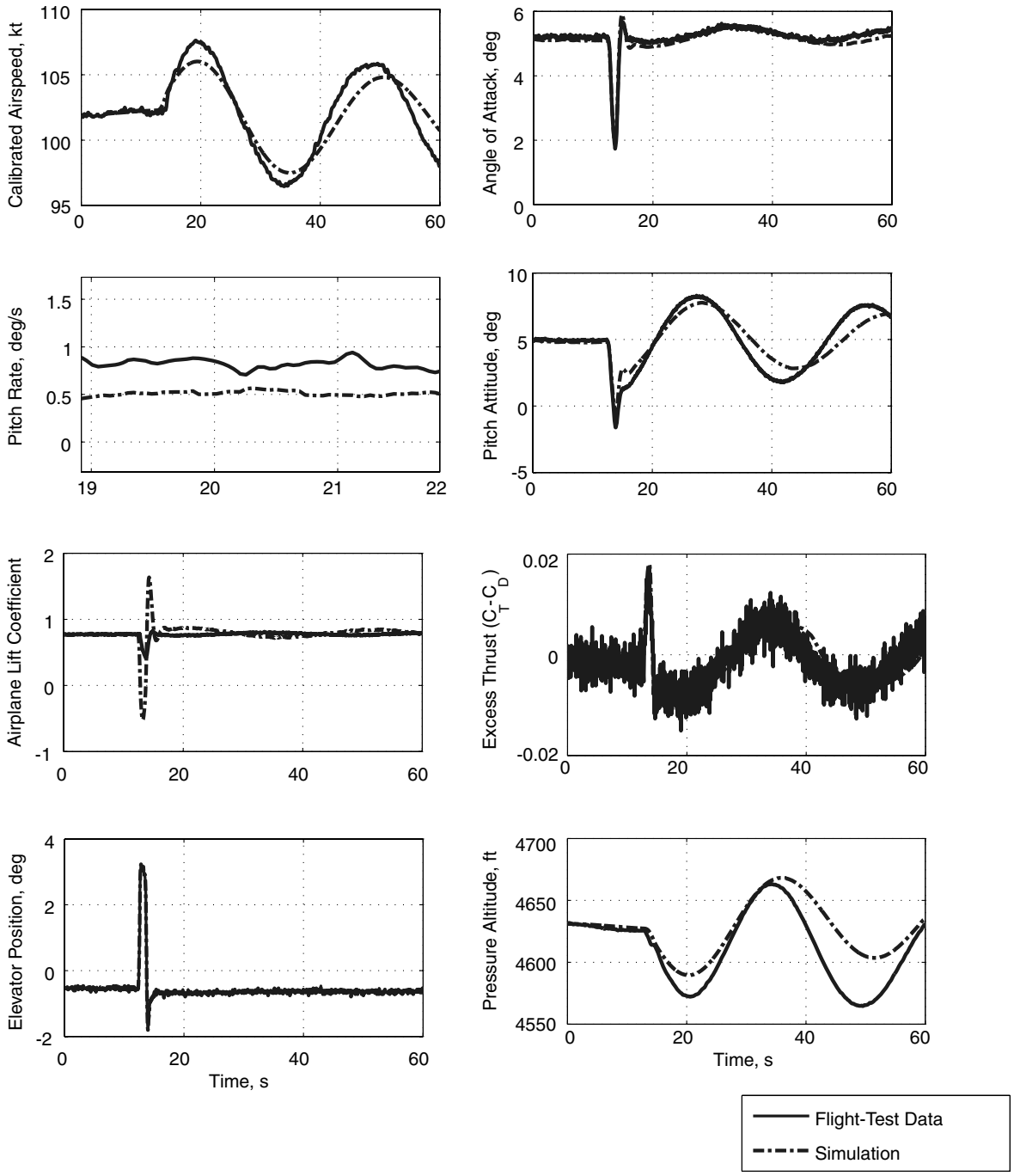

Fig. 5 Elevator singlet verification maneuver responses.

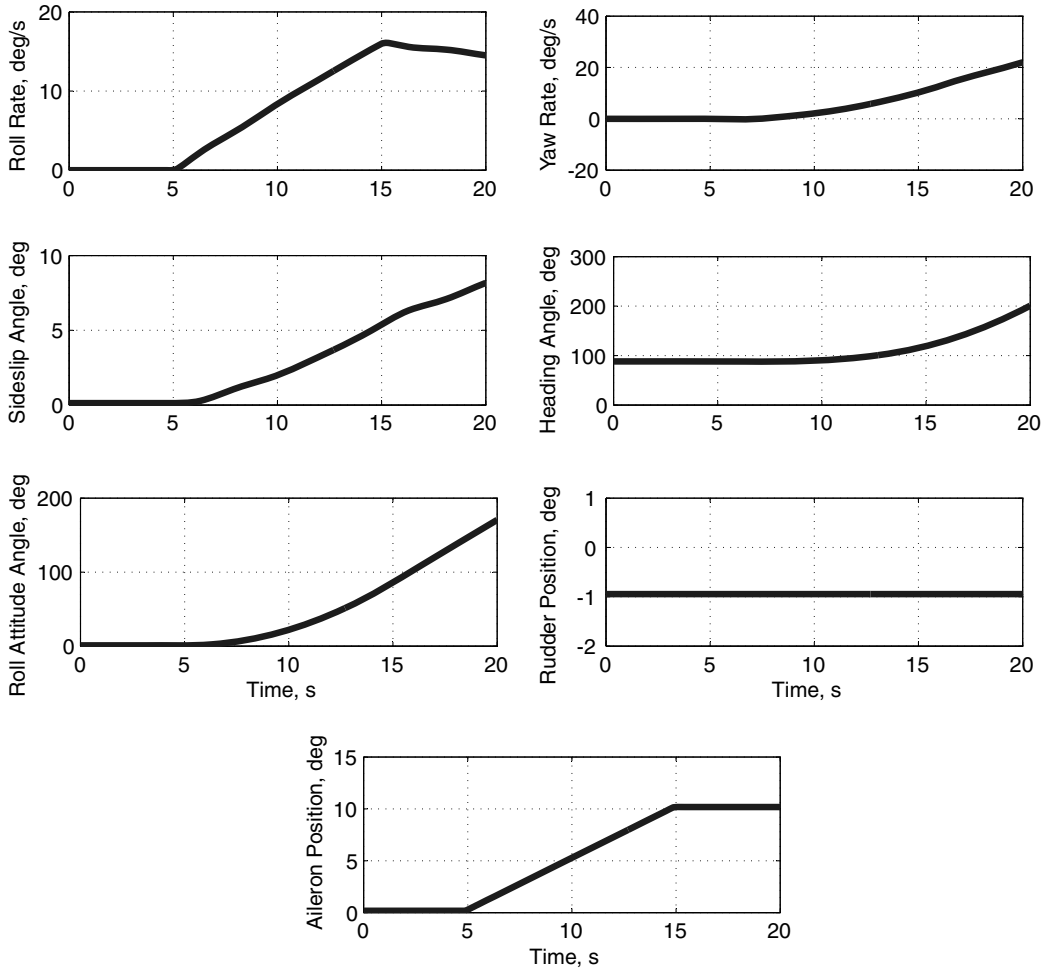

Fig. 6 Ramp aileron input responses.

factors are then applied, and the iced lift or iced drag is then subtracted from the clean lift and drag equations, as seen in Eq. (25), where the "ice" subscript denotes the right wing with ice applied and the Δ indicates the difference between the left and right wing halves.

$$\Delta C_{L_{\text{ice}}} = \tfrac{1}{2}C_{L_{\text{ice}}} - \tfrac{1}{2}C_L \qquad \Delta C_{D_{\text{ice}}} = \tfrac{1}{2}C_D - \tfrac{1}{2}C_{D_{\text{ice}}} \tag{25}$$

The difference in the lift coefficient and drag coefficient is then dimensionalized as induced moment due to ice accretions by Eqs. (26) and (27), where d_{mgc} denotes the distance along the body X axis from the mean geometric chord to the airplane centerline.

$$\Delta L_{\text{ice}} = \frac{\Delta C_{L_{\text{ice}}} \bar{q} S d_{\text{mgc}}}{I_{xx}} \tag{26}$$

$$\Delta N_{\text{ice}} = \frac{\Delta C_{D_{\text{ice}}} \bar{q} S d_{\text{mgc}}}{I_{zz}} \tag{27}$$

These induced moments are then integrated into the state-space equations described in previous sections by adding a disturbance term to the state-space formulation as seen in Eq. (28).

$$\dot{\boldsymbol{X}} = E^{-1}A\boldsymbol{X} + E^{-1}\boldsymbol{B}\boldsymbol{U} + G\boldsymbol{W} \tag{28}$$

The disturbance term encompassing the induced moments due to ice accretion is represented by Eq. (29)

$$G\boldsymbol{W} = \begin{bmatrix} 0 & 0 \\ 0 & 0 \\ 0 & 0 \\ 0 & 0 \\ 0 & 0 \\ \Delta L_{\text{ice}} & 0 \\ 0 & \Delta N_{\text{ice}} \\ 0 & 0 \\ 0 & 0 \end{bmatrix} \begin{bmatrix} 1 \\ 1 \end{bmatrix} \tag{29}$$

where $\boldsymbol{W}$ corresponds to a constant step disturbance. To remain within the scope of this research, the induced moments are calculated

Table 5 Level right bank validation maneuver flight conditions and trim conditions

Altitude, ft	Calibrated airspeed, kt	Dynamic pressure, lbs/ft^2	Weight, lb	Center of gravity, $\bar{c}$	α_1, deg	β_1, deg	δ_{a_1}, deg	δ_{r_1}, deg
15,000	135	35.219	8402	0.289	5.51	0.13	0.18	−0.95

Table 6 Lateral/directional verification maneuver flight conditions and trim conditions

Altitude, ft	Calibrated airspeed, kt	Dynamic pressure, lbs/ft^2	Weight, lb	Center of gravity, $\bar{c}$	α_1, deg	β_1, deg	δ_{a_1}, deg	δ_{r_1}, deg
15, 000	135	40.97	8402	0.289	1.28	0.13	0.18	−0.95

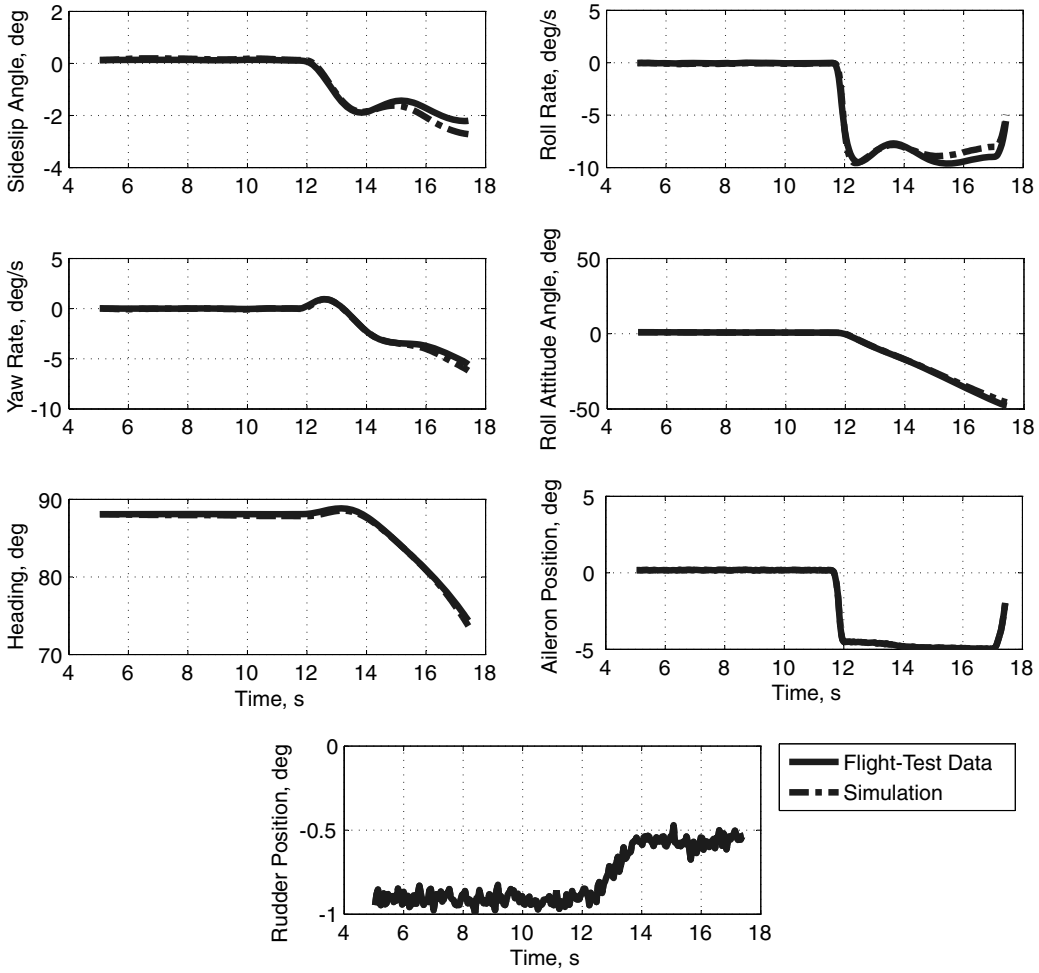

Fig. 7 Aileron singlet verification maneuver responses.

for the first time step and held constant from then on, thus G is time invariant.

V. Simulation Validation and Verification

To validate the mathematics and physics of the airplane model and simulation, a series of standard maneuvers were performed to determine if it responds correctly and consistently to control inputs for a conventional airplane configuration with conventional controls. Six verification maneuvers were performed and compared with flight-test data obtained from the Cessna 208B Super Cargomaster to ensure that the simulation accurately represents a Cessna 208B Super Cargomaster. Flight-test data were available for only a limited set of maneuvers, from which the verification maneuvers were selected.

A. Longitudinal Validation

The airplane model was subjected to several validation maneuvers to determine if it responds correctly and consistently to control inputs. For brevity, only one maneuver, a level acceleration to validate the longitudinal dynamics, is reproduced here. It consists of a level acceleration from trim with the throttle as the only modulating control. Flight and trim conditions for the longitudinal dynamics validation maneuver are shown in Table 3. This maneuver should result in an increase in speed, an increase in altitude, and the airplane pitching nose up. The level acceleration is performed by holding the elevator at a constant trim deflection and changing the throttle control, or power lever angle (PLA). For this airplane, the idle position is 1.3 in., whereas the maximum throttle position is 3.7 in. This simulation starts from a trim throttle position of 2.45 in. and changes the position from 2.45 to 3.7 in. over a period of 20 s. Results are only plotted up to 12 s because the response of the airplane at the given flight conditions is adequately represented in that amount of

Table 9 Trim angle of attack for the iced airplane

Case	$\alpha_{1_{ice}}$, deg
1	7.22
2	7.22
3	10.00

Table 7 Flight and trim conditions for cases 1 and 2 for the clean airplane

Altitude, ft	Calibrated airspeed, kt	Dynamic pressure, lbs/ft^2	Weight, lb	Center of gravity, $\bar{c}$	α_1, deg	β_1, deg	δ_{e_1}, deg	δ_{a_1}, deg	δ_{r_1}, deg
15,000	105.5	35.22	8402	0.34	6.21	0.0	−1.52	0.18	−0.95

Table 8 Flight and trim conditions for case 3 for the clean airplane

Altitude, ft	Calibrated airspeed, kt	Dynamic pressure, lbs/ft^2	Weight, lb	Center of gravity, $\bar{c}$	α_1, deg	β_1, deg	δ_{e_1}, deg	δ_{a_1}, deg	δ_{r_1}, deg
15,000	95	35.22	8704	0.34	8.35	0.0	0.0	0.18	−0.95

time. The flight conditions for the test are shown in Table 2 and the responses in Fig. 4.

The airspeed response in Fig. 4 shows an almost steady increase once PLA starts to shift at 3 s, and the angle-of-attack response decreases correspondingly. Altitude increases as well as the lift coefficient and drag coefficient initially, as expected. The elevator time history simply shows that it is being held constant while throttle is increased. These results are reasonably accurate with respect to the physics involved and indicate that the airplane model responds properly to a throttle input. The other validation maneuvers (not shown) also supported the conclusion of correct validation.

B. Longitudinal Verification

For brevity, only one longitudinal maneuver is reproduced here. The maneuver is an elevator singlet, which excites the short period mode and verifies the longitudinal dynamical model. Flight and trim conditions for the longitudinal dynamics verification maneuver are shown in Table 4. The simulation and flight-test airplanes are both subjected to an elevator singlet to excite short period and (to a lesser extent) phugoid responses. To ensure the greatest accuracy in comparing the simulation to the flight-test data, the elevator deflection history recorded from the flight test was used directly as the control input for the simulation. The time histories of the states, altitude, C_L, C_D, and elevator deflection for both the flight-test data and the simulation are shown in Fig. 5. The airspeed responses of both the flight-test airplane and the simulation are similar, with a maximum airspeed error at any given instant of time of 2.0%. The angle-of-attack responses also show similarities, with a maximum error of 3.0%. The error for the pitch rate appears high because the recorded flight-test data do not provide a smooth time history and thus the flight-test data appear to oscillate about the simulation time history. The nondimensionalized thrust minus the airplane drag coefficient (row 3, column 2 of Fig. 5) has a constant offset of about 0.0175, because the value used for C_{D_0} was based on drag polars, not direct calculation. The simulation airplane lift coefficient, however, shows that the simulation is much more responsive to the elevator input than the flight-test data suggest, but the response later in the time history is similar. Finally, the altitude time history again shows

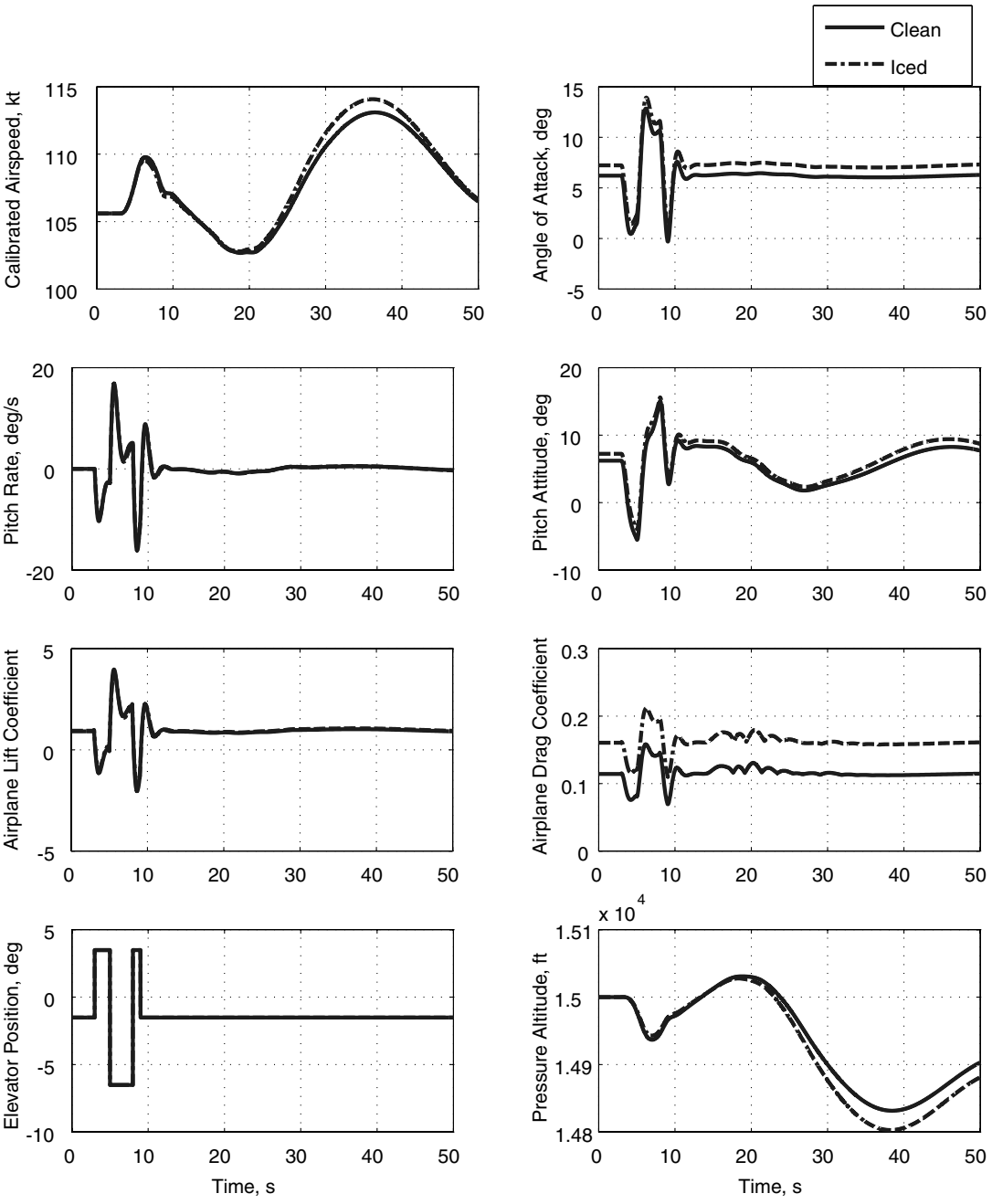

Fig. 8 Case 1: doublet and triplet maneuvers longitudinal states for clean and fully iced airplane.

the similarity between the flight-test data and the simulation. The difference is greatest at about 50 s into the simulation with an error of 1.0% between them.

Mismatches or errors noted in Fig. 5 between the flight-test data and the simulation model arise from several sources. The first is that the simulation is an LTI model of a highly nonlinear time-variant system, and so small changes in the engine performance or control surface deflections are not accounted for in the model. Also, the model does not take into account external perturbations such as gusts that probably affected the flight-test airplane to some extent during the test flights. Despite these inaccuracies, the response is generally as expected, and the longitudinal model is judged to be acceptable as an accurate representation of the airplane, within the limitations and accuracies of the methods used to construct the model.

C. Lateral/Directional Validation

For brevity, only one maneuver, a level right bank to validate the lateral dynamics, is reproduced here. It consists of a level right bank from trim with the aileron deflection as the only modulating control. This maneuver should result in an increase in the roll rate, an increase in the yaw rate, and an increase in the sideslip angle due to adverse yaw. The level right bank maneuver is performed by holding the rudder at a constant trim deflection and changing the aileron deflection. This simulation starts from a trim aileron deflection of 0.18 deg and changes from 0.18 to 5.18 deg over a period of 10 s. Results are only plotted up to 20 s because the response of the airplane at the given flight conditions is adequately represented in that amount of time. The flight conditions for the test are shown in Table 5 and the responses in Fig. 6.

The bank angle or roll attitude response in Fig. 6 shows an almost steady increase once the aileron deflection starts to shift at 5 s, and the heading angle response increases correspondingly. The roll rate increases as well as the sideslip angle and the yaw rate due to adverse yaw, as expected. The rudder time history simply shows that it is being held constant while aileron deflection is increased. These results are reasonably accurate with respect to the physics involved and indicate that the airplane model responds properly to an aileron input. The other validation maneuvers (not shown) also supported the conclusion of correct validation.

D. Lateral/Direction Verification

Flight and trim conditions for the lateral/directional dynamics verification maneuver are shown in Table 6.

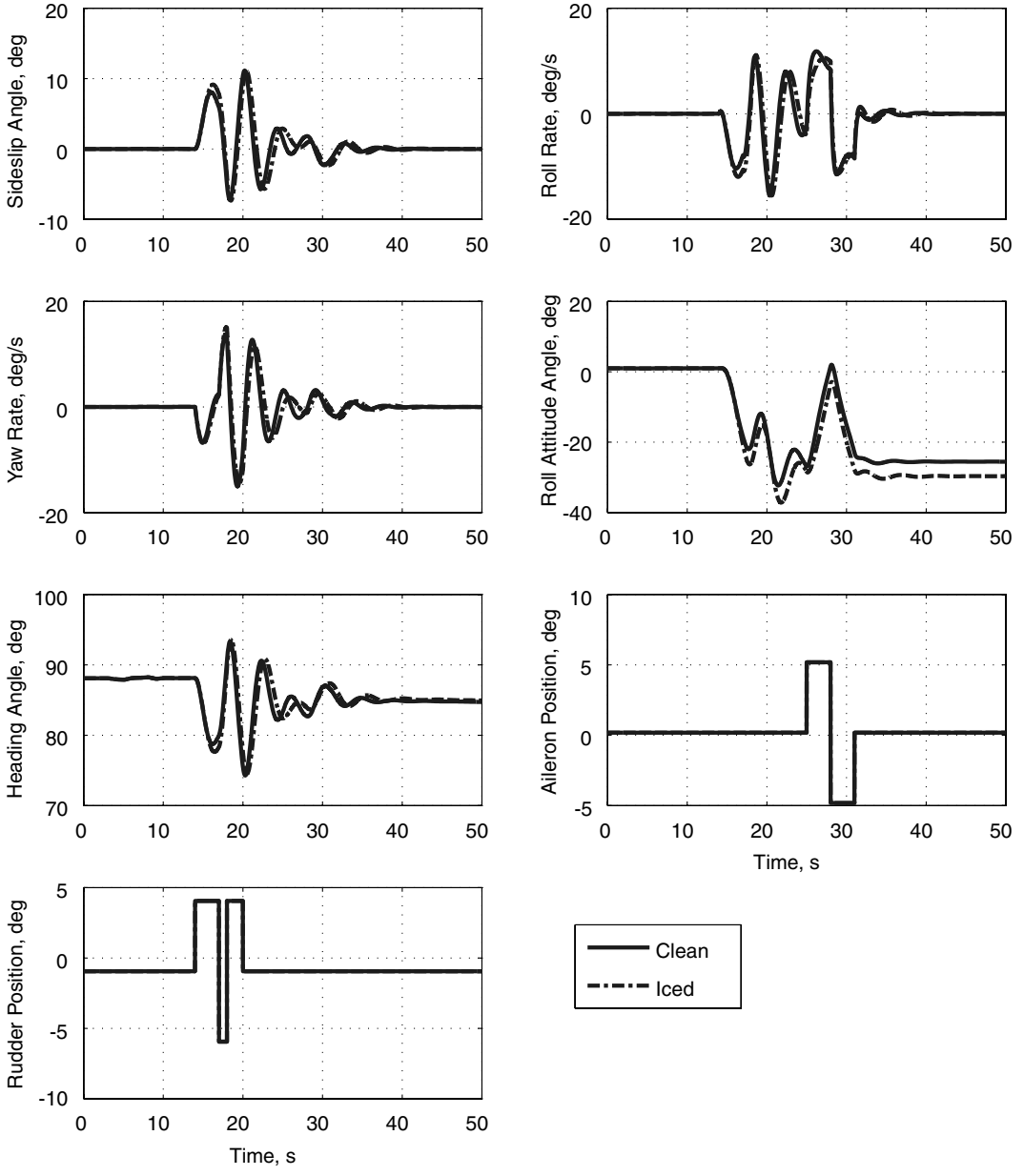

Fig. 9 Case 1: doublet and triplet maneuvers lateral/directional states for clean and fully iced airplane.

The simulation and flight-test airplanes are both subjected to an aileron singlet to excite Dutch roll and (to a lesser extent) roll and spiral responses. To ensure the greatest accuracy in comparing the simulation to the flight-test data, the aileron and rudder deflection histories recorded from the flight test were used directly as the control inputs for the simulation. The time histories of the states and control surface deflections for both the flight-test data and the simulation are shown in Fig. 7. Examination of the sideslip angle, roll rate, yaw rate, roll attitude, and heading shows that the simulation responds very closely to the test airplane. There are minimal errors in each on the order of perhaps 2%.

Mismatches or errors noted in Fig. 7 between the flight-test data and the simulation model arise from several sources as noted previously. The first is that the simulation is a linear time-invariant model of a highly nonlinear time-variant system, and so small changes in the engine performance or control surface deflections are not accounted for in the model. Also, the model does not take into account external perturbations such as gusts that probably affected the flight-test airplane to some extent during the test flights. Despite these inaccuracies, the response is generally as expected, and the lateral/directional model is judged to be acceptable as an accurate representation of the airplane, within the limitations and accuracies of the methods used to construct the model as stated in previous sections.

VI. Simulation Examples

The simulation was used to evaluate several control inputs and uneven icing scenarios for the purpose of determining the change in both the dynamic response and performance due to various ice accretion distributions. The first example consists of a series of doublet and triplet maneuvers presented to demonstrate the prediction of icing effects on airplane states. The first maneuver is an elevator triplet, and the second is a rudder triplet followed closely by an aileron doublet. Also presented is a case with ice on the right half of the wing only in cruise and a case with ice on the right half of the wing in a maximum powered climb. The data presented in Table 2 represents mixed icing conditions [6]. These are the degradation factors that are applied to the stability and control derivatives shown in Eq. (19), and they indicate how much the lift decreases, drag increases, longitudinal stability decreases, and lateral stability decreases for each derivative in the case of evenly accreted ice on the whole airplane and how much lift decreases and drag increases for the case of uneven accretion of ice on the right half of the wing.

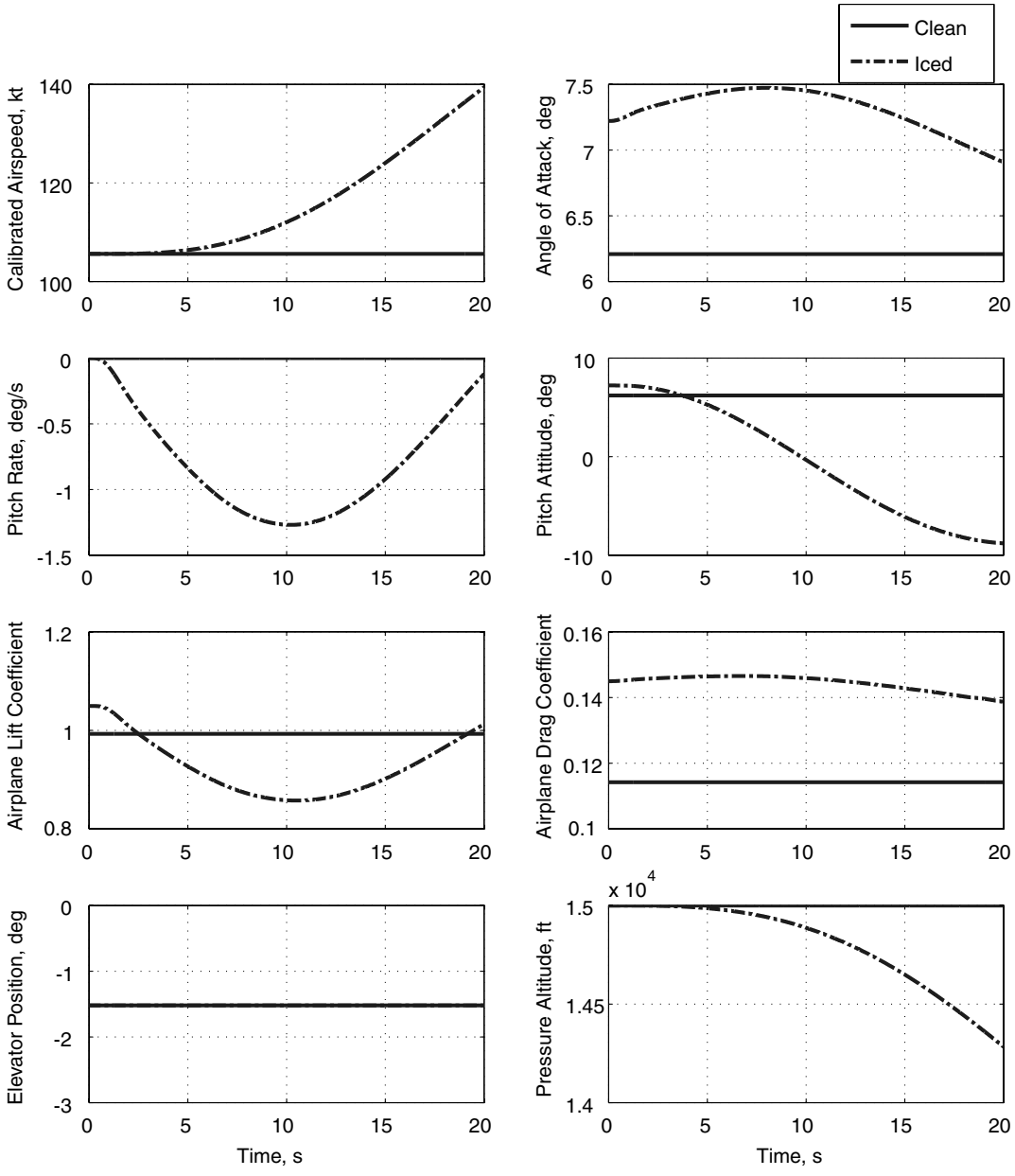

Fig. 10 Case 2: longitudinal states for clean and asymmetric iced airplanes in cruise.

Subtracting the absolute value of each percentage from unity and applying it to the derivative indicated will effectively modify the airplane model for icing. In addition, an increase of 15% was applied to the total drag, based on data obtained for the Twin Otter that shows an increase in drag of anywhere from approximately 5 to 30% [6,27]. For the purpose of direct comparison, the weight and airspeed are the same for each case except for the climb, shown in Table 7. Flight conditions for the climb maneuver are shown in Table 8. For both the clean and iced airplanes in climb, calibrated airspeed is maintained at the recommended value of 95 kt to achieve the maximum rate of climb for the Cessna 208B [25].

Flight and trim conditions for the iced airplane are all the same as those listed in Tables 7 and 8 except for the angle of attack. The angle of attack is retrimmed to compensate for the decrease in lift and increase in drag due to ice accretions. The trim angles of attack for the iced airplane are listed in Table 9.

A. Case 1: Doublet and Triplet Maneuvers, Fully Iced Configuration

This case investigates a series of doublet and triplet maneuvers consisting of an elevator 2-3-1 triplet followed later by a rudder 3-1-2 triplet and an aileron doublet and tracked for a period of 50 s. This example represents a configuration with evenly distributed amounts of ice accretions on both the wing and horizontal tail as well as between wing halves. For case 1, "fully iced" means that the full factors listed in Table 2 are applied to their respective stability and control derivatives. This is effectively the "worst-case" scenario for an evenly iced airplane.

Figures 8 and 9 show that the rudder triplet follows about 5 s after the elevator triplet with the aileron doublet following close behind the rudder triplet, and that both the clean and iced airplanes are subjected to the same control inputs. The airplane is close to trim for the cruise condition, which allows the differences between the clean and iced configurations during the maneuvers to be easily seen without undue oscillations.

The ice accretions are known to alter the shape of the carefully engineered airfoil, thus decreasing its effectiveness at generating lift. Studies conducted at the University of Illinois on various airfoils with different types of ice accretions support this observation [5]. Also supported by these studies is an increase in drag caused by the ice accretions forming a horn or projection on the leading edge of the wing, thereby disrupting the airflow. This is shown in the airplane drag coefficient time history of Fig. 8, in which the drag is almost 460 counts greater for the iced case than the clean case. In terms of airplane drag, this count increase is very large.

The effect of the worst-case scenario icing as shown in Figs. 8 and 9 demonstrates one of the major hazards of an iced airplane: it does not respond to pilot commands in quite the same manner as a clean airplane. Though the effect of evenly distributed ice is not extreme, small differences between the iced and non-iced configurations do

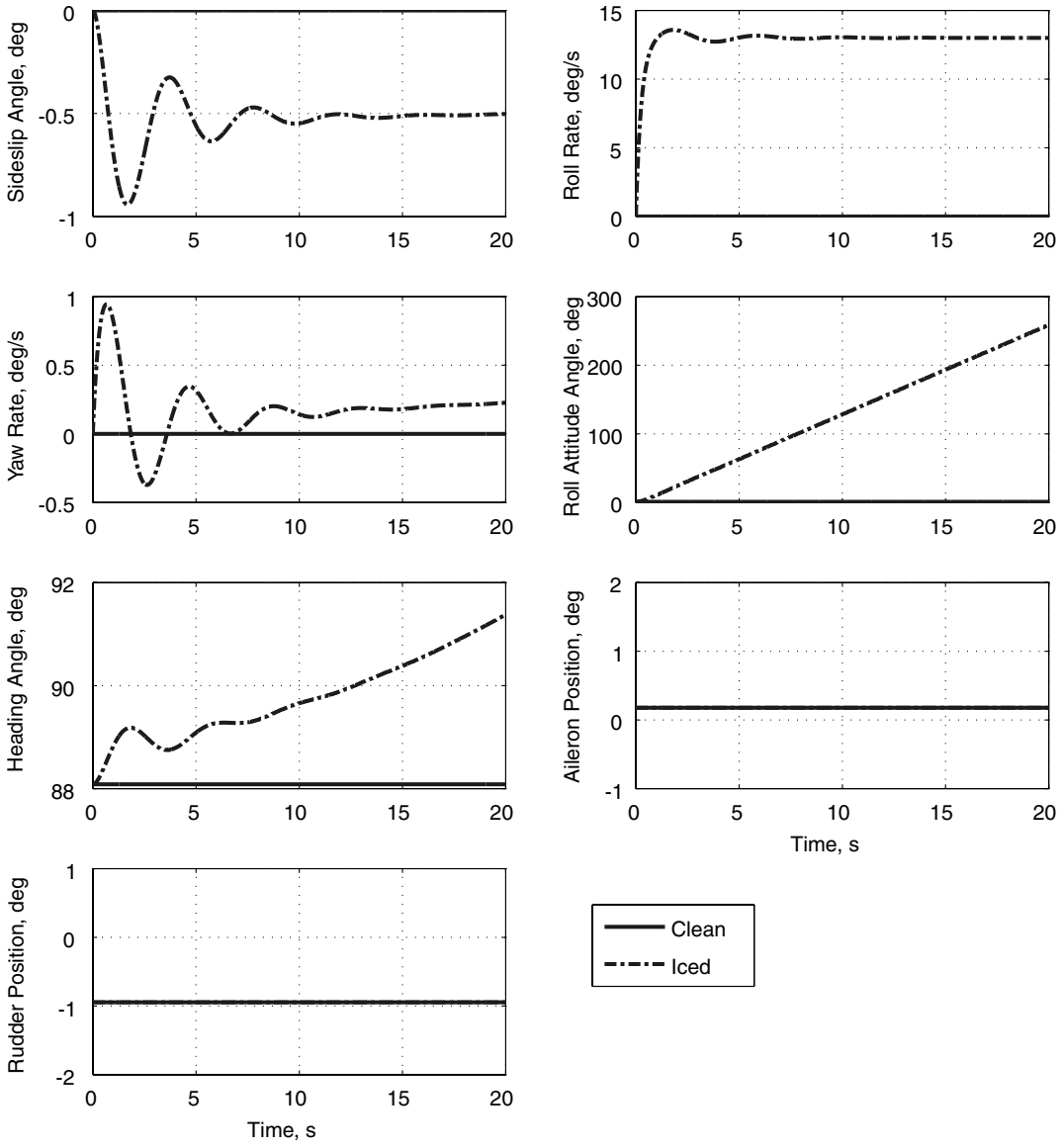

Fig. 11 Case 2: lateral/directional states for clean and asymmetric iced airplanes in cruise.

appear. The angle of attack for the iced airplane is about 1.2 deg greater than the clean airplane throughout the maneuvers. However, it is not large enough for a stall to occur. The pitch rate, roll rate, and yaw rate responses only show slight changes in the iced configuration. There are also slight differences in airspeed and altitude, and it is important to note that altitude begins to decrease as the airplane settles into a positive roll attitude angle with the iced airplane gaining speed and losing altitude faster than in the clean case. Despite all the motion, the oscillations of both the clean and iced airplanes show signs of damping out, illustrating that the iced airplane remains inherently stable when the ice is distributed evenly.

B. Case 2: Uneven Asymmetric Icing in Cruise, Fully Iced Configuration

This case represents an airplane with worst-case ice accretions on only one half of the wing. The iced airplane is trimmed as if ice accreted evenly on the whole wing, and then the de-icing device malfunctions such that ice is cleared from only one half of the wing. As a result of this uneven icing and the resulting differences in lift and drag between the iced half and non-iced half of the wing, an ice-induced rolling moment and yawing moment develop. This maneuver consists of allowing the airplane to respond to these lateral/directional moments and noting the roll-off tendencies of the iced airplane without any corrective control inputs. This open-loop simulation does not have a human pilot to correct for these induced moments, and in known icing conditions the autopilot would not be used in most cases.

Figures 10 and 11 show that the iced airplane immediately responds to the induced moments whereas the clean airplane remains at trim. Both the roll rate and yaw rate indicate that the airplane has become unstable and is no longer within the linear range of the simulation. This happenstance explains the response in the longitudinal states. The drag increases by over 300 counts. The altitude begins to decrease at an increasing rate as the aircraft nose angles downward, as indicated by the lateral/directional responses. The airspeed of the iced airplane increases, as expected, as it dives. The simulation ends at 20 s because, by that point, the iced airplane is outside the linear range. The induced positive rolling moment and yawing moment result in the airplane flipping over within 15 s. Roll rate indicates that it will continue to roll at a near constant rate. The heading angle is quickly changing, and the yaw rate indicates that the

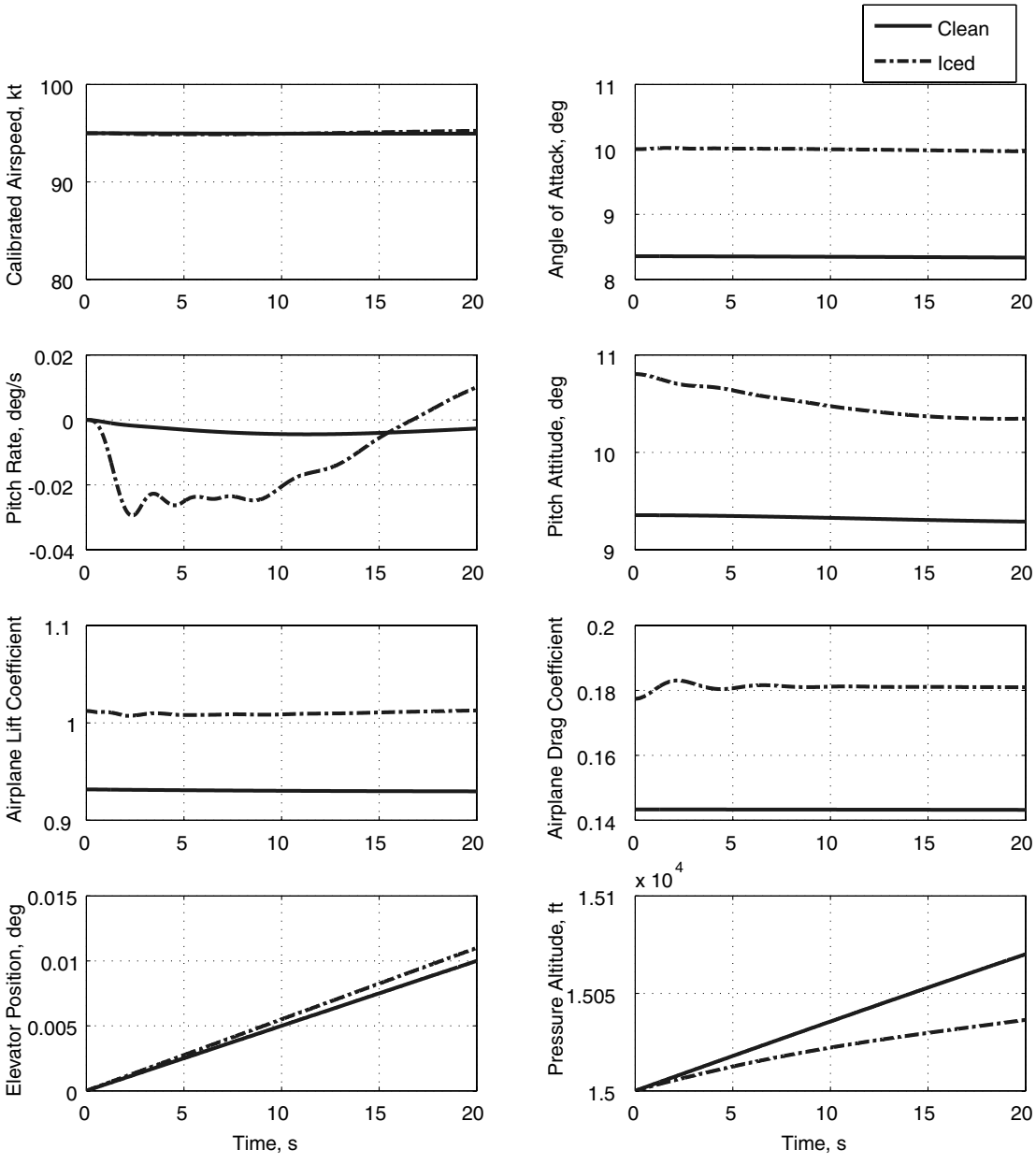

Fig. 12 Case 3: longitudinal states for clean and asymmetric iced airplanes in max powered climb.

change is going to continue at a slightly increasing rate as time progresses. All of these responses are effectively summarized by noting that the time to double is about 5 s. For many airplanes of this class, imbalance in ice distribution can quickly lead to a departure from controlled flight.

C. Case 3: Uneven Asymmetric Icing in a Climb, Fully Iced Configuration

This case represents an airplane in the initial stages of a climb maneuver with worst-case ice accretions on only one half of the wing. Similar to the previous case, the airplane is initially trimmed as if the iced airplane is fully and evenly iced. Then, due to either a malfunctioning de-icing system or some other phenomenon, the ice is cleared from the left half of the wing but not the right. The maneuver consists of a time-varying elevator input for the climb, allowing the airplane to respond to the ice-induced lateral/directional moments, and noting roll-off and other tendencies.

Figure 12 shows the airplane climbing while maintaining airspeed with predefined elevator deflection profiles as functions of time for the clean and iced airplanes. The drag for the iced airplane is almost 350 counts larger than that for the clean airplane. The pitch attitude angle begins a decreasing trend toward the end of the 20 s interval. There is a significant difference in altitude between the clean and iced airplanes. This difference is the first indication that the airplane is not responding properly and is departing from controlled flight.

Figure 13 better illustrates the probable departure of the airplane. The heading angle is increasing more rapidly than in the previous case as described by the larger yaw rate. The roll attitude angle does not respond as violently as that of the previous case. The reason is that, with the iced airplane trimmed at a higher angle of attack, there is less of a lift differential between the wing halves. Therefore, there is a smaller induced rolling moment. Similar to the previous case, the time to double is small, at about 3 s. All of these responses indicate the likelihood of a full departure from controlled flight, as well as a departure from the linear realm of this simulation.

VII. Conclusions

An analysis method using flight data, wind-tunnel data, and the United States Air Force Data Compendium was developed to create a basic but reasonably detailed and accurate methodology for evaluating the effects of ice accretion on the coupled 6-degree-of-freedom dynamics of light airplanes. The component buildup method was used to implement icing effects on one half of the wing alone and on the combined wing and horizontal tail using icing data

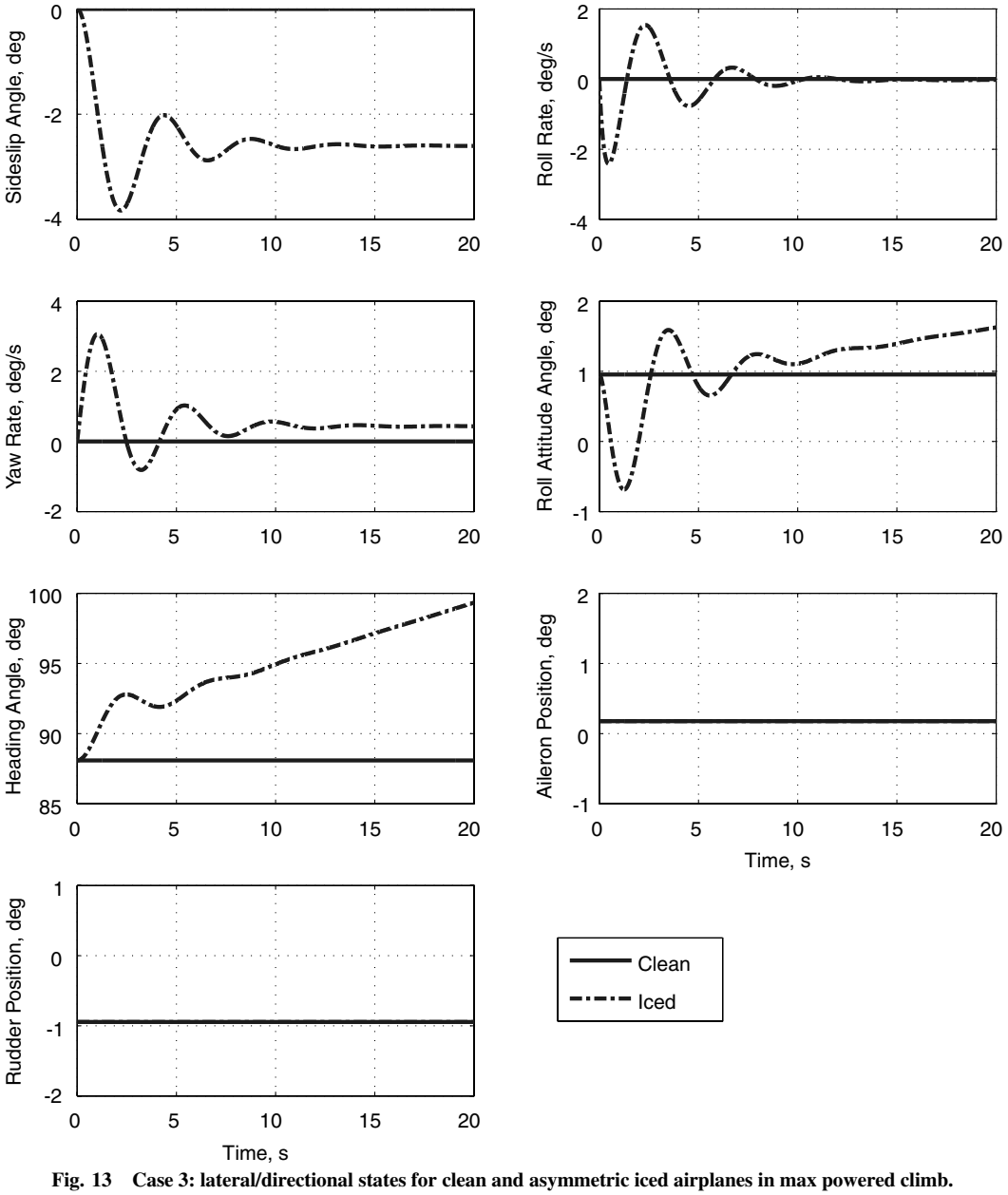

Fig. 13 Case 3: lateral/directional states for clean and asymmetric iced airplanes in max powered climb.

from similar light airplanes. The icing data used were obtained empirically and modified for the airplane configuration considered. A linear time-invariant state-space model of the coupled longitudinal and lateral/directional model of a representative light airplane was developed and used for nonreal-time simulation to evaluate icing effects on stability and control characteristics, in addition to effects on roll-off tendencies. Validation of the simulation model was conducted using several basic maneuvers, and verification was conducted using flight-test data for the same airplane as the simulation. Numerical examples consisting of doublet and triplet maneuvers and two uneven icing roll-off assessments in various levels of icing, one example in cruise and one in a climb, were evaluated.

Based on the results presented in the paper, it is concluded that the coupled linear state-space model representation, discrete simulation model, and inclusion of simplified icing effects appear to be an adequate tool for basic coupled icing dynamics and performance analysis for the maneuvers investigated. Verification results to the flight data that is available showed good agreement for the maneuvers investigated here. Qualitatively, the simulation results show that evenly distributed ice caused the airplane to respond slightly differently, but the evenly iced airplane remains inherently stable for the longitudinal and lateral/directional maneuvers investigated. Finally, for the uneven accretion comparisons of the iced airplane to the clean airplane, allowing the iced airplane to respond to ice-induced moments, simulation results showed an adverse affect on airplane stability. The cruise case had a 300 count drag increase and exhibited a departure from controlled flight with a time to double of 5 s. The climb case had a 350 count drag increase and also exhibited a departure from controlled flight with a time to double of 3 s.

Acknowledgment

This research is funded by the Aeronautical and Educational Services Company, under grant number C05-00356. The technical monitor is Donald T. Ward. The authors gratefully acknowledge this support.

References

[1] Anon., "Annual Review of Aircraft Accident Data: U.S. General Aviation, Calendar Year 1997," National Transportation Safety Board, Washington, D. C., 2003.

[2] Anon., "Annual Review of Aircraft Accident Data: U.S. General Aviation, Calendar Year 1998," National Transportation Safety Board, Washington, D. C., 2003.

[3] Anon., "Annual Review of Aircraft Accident Data: U.S. General Aviation, Calendar Year 1999," National Transportation Safety Board, Washington, D. C., 2003.

[4] Anon., "Annual Review of Aircraft Accident Data: U.S. General Aviation, Calendar Year 2000," National Transportation Safety Board, Washington, D. C., 2004.

[5] Gurbacki, H., and Bragg, M., "Unsteady Aerodynamic Measurements on an Iced Airfoil," AIAA Paper 2002-0241, Jan. 2002.

[6] Bragg, M., Hutchison, T., Merret, J., Oltman, R., and Pokhariyal, D., "Effect of Ice Accretion on Aircraft Flight Dynamics," AIAA Paper 2000-0360, Jan. 2000.

[7] Sharma, V., Voulgaris, P., and Frazzoli, E., "Aircraft Autopilot Analysis and Envelope Protection for Operation Under Icing Conditions," *Journal of Guidance, Control, and Dynamics*, Vol. 27, No. 3, 2004, pp. 454–465.

[8] Sibilski, K., Lasek, M., Ladyzynska-Kozdras, E., and Maryniak, J., "Aircraft Climbing Flight Dynamics With Simulated Ice Accretion," AIAA Paper 2004-4948, Aug. 2004.

Appendix: Linear State-Space Models of Clean Cessna 208B Super Cargomaster

The linear models of the Cessna 208B for case 1 and 2 are based upon a steady, level, 1-g-trimmed flight condition at a calibrated airspeed of 105.5 kt and an altitude of 15,000 ft. The trim values are $\alpha_1 = 6.21$ deg, $\delta_{e_1} = -1.52$ deg, and $\mathrm{PLA}_1 = 2.45$ deg.

$$\begin{bmatrix} \dot{u} \\ \dot{\alpha} \\ \dot{q} \\ \dot{\theta} \\ \dot{\beta} \\ \dot{p} \\ \dot{r} \\ \dot{\phi} \\ \dot{\psi} \end{bmatrix} = \begin{bmatrix} -0.04 & 18.08 & 0 & -31.99 & -2.86 & 0 & 0 & 0 & 0 \\ -0.001 & -0.92 & 0.98 & -0.02 & 0 & 0 & 0 & 0.02 & 0 \\ -0.0005 & -7.04 & -1.57 & 0 & 0 & 0 & 0 & 0 & 0 \\ 0 & 0 & 1.00 & 0 & 0 & 0 & -0.02 & 0 & 0 \\ 0 & 0 & 0 & 0 & -0.17 & 0.001 & -1.00 & 0.0006 & 0 \\ 0 & 0 & 0 & 0 & -5.96 & -4.10 & 0.77 & 0 & 0 \\ 0 & 0 & 0 & 0 & 2.16 & -0.19 & -0.52 & 0 & 0 \\ 0 & 0 & 0.002 & 0 & 0 & 1 & 0.11 & 0 & 0 \\ 0 & 0 & 0.02 & 0 & 0 & 0 & 1.01 & 0 & 0 \end{bmatrix} \begin{bmatrix} u \\ \alpha \\ q \\ \theta \\ \beta \\ p \\ r \\ \phi \\ \psi \end{bmatrix} + \begin{bmatrix} -0.45 & 0 & 0 \\ -0.09 & 0 & 0 \\ -7.90 & 0 & 0 \\ 0 & 0 & 0 \\ 0 & 0 & 0.04 \\ 0 & 8.99 & 1.10 \\ 0 & -0.07 & -2.64 \\ 0 & 0 & 0 \\ 0 & 0 & 0 \end{bmatrix} \begin{bmatrix} \delta_e \\ \delta_a \\ \delta_r \end{bmatrix}$$

The linear model of the Cessna 208B for case 3 is based upon a steady, level, 1-g-trimmed flight condition at a calibrated airspeed of 95 kt and an altitude of 15,000 ft. The trim values are $\alpha_1 = 8.35$ deg, $\delta_{e_1} = 0$ deg, and $\mathrm{PLA}_1 = 1.9$ deg.

$$\begin{bmatrix} \dot{u} \\ \dot{\alpha} \\ \dot{q} \\ \dot{\theta} \\ \dot{\beta} \\ \dot{p} \\ \dot{r} \\ \dot{\phi} \\ \dot{\psi} \end{bmatrix} = \begin{bmatrix} -0.10 & 19.22 & 0 & -31.75 & -2.48 & 0 & 0 & 0 & 0 \\ -0.002 & -0.72 & 0.97 & -0.03 & 0 & 0 & 0 & 0.02 & 0 \\ -0.0003 & -2.53 & -1.32 & 0 & 0 & 0 & 0 & 0 & 0 \\ 0 & 0 & 1.00 & 0 & 0 & 0 & -0.02 & 0 & 0 \\ 0 & 0 & 0 & 0 & -0.17 & 0.04 & -1.00 & 0.0008 & 0 \\ 0 & 0 & 0 & 0 & -4.99 & -3.81 & 0.72 & 0 & 0 \\ 0 & 0 & 0 & 0 & 1.85 & -0.18 & -0.50 & 0 & 0 \\ 0 & 0 & 0.003 & 0 & 0 & 1 & 0.16 & 0 & 0 \\ 0 & 0 & 0.02 & 0 & 0 & 0 & 1.01 & 0 & 0 \end{bmatrix} \begin{bmatrix} u \\ \alpha \\ q \\ \theta \\ \beta \\ p \\ r \\ \phi \\ \psi \end{bmatrix} + \begin{bmatrix} -0.39 & 0 & 0 \\ -0.09 & 0 & 0 \\ -5.28 & 0 & 0 \\ 0 & 0 & 0 \\ 0 & 0 & 0.04 \\ 0 & 7.52 & 0.92 \\ 0 & -0.07 & -2.25 \\ 0 & 0 & 0 \\ 0 & 0 & 0 \end{bmatrix} \begin{bmatrix} \delta_e \\ \delta_a \\ \delta_r \end{bmatrix}$$

[9] Reehorst, A., Chung, J., Potapczuk, M., and Choo, Y., "Study of Icing Effects on Performance and Controllability of an Accident Aircraft," *Journal of Aircraft*, Vol. 37, No. 2, 2000, pp. 253–259.

[10] Lee, S., and Bragg, M., "Experimental Investigation of Simulated Large-Droplet Ice Shapes on Airfoil Aerodynamics," *Journal of Aircraft*, Vol. 36, No. 5, 1999, pp. 844–850.

[11] Broeren, A., Addy, H. E., Jr., and Bragg, M., "Effect of Intercycle Ice Accretions on Airfoil Performance," *Journal of Aircraft*, Vol. 41, No. 1, 2004, pp. 165–174.

[12] Whalen, E., and Bragg, M., "Aircraft Characterization in Icing Using Flight-Test Data," *Journal of Aircraft*, Vol. 42, No. 3, 2005, pp. 792–794.

[13] Broeren, A., and Bragg, M., "Effect of Airfoil Geometry on Performance with Simulated Intercycle Ice Accretions," *Journal of Aircraft*, Vol. 42, No. 1, 2005, pp. 121–130.

[14] Lee, S., and Bragg, M. B., "Investigation of Factors Affecting Iced-Airfoil Aerodynamics," *Journal of Aircraft*, Vol. 40, No. 3, 2003, pp. 499–508.

[15] Bragg, M., "Aircraft Aerodynamic Effects Due to Large Droplet Ice Accretions," AIAA Paper 96-0932, Jan. 1996.

[16] Lu, B., and Bragg, M., "Airfoil Drag Measurement with Simulated Leading-Edge Ice Using the Wake Survey Method," AIAA Paper 2003-1094, Jan. 2003.

[17] Broeren, A., Addy, H. E., Jr., and Bragg, M., "Flowfield Measurements About an Airfoil with Leading-Edge Ice Shapes," AIAA Paper 2004-0559, Jan. 2004.

[18] Bragg, M., Perkins, W., Sarter, N., Basar, T., Voulgaris, P., Gurbacki, H., Melody, J., and McCray, S., "An Interdisciplinary Approach to Inflight Aircraft Icing Safety," AIAA Paper 98-0095, Jan. 1998.

[19] Bragg, M., Basar, T., Perkins, W., Selig, M., Voulgaris, P., Melody, J., and Sarter, N., "Smart Icing Systems for Aircraft Icing Safety," AIAA Paper 2002-0813, Jan. 2002.

[20] Melody, J. W., Basar, T., Perkins, W. R., and Voulgaris, P. G., "Parameter Identification for Inflight Detection and Characterization of Aircraft Icing," *Control Engineering Practice*, Vol. 8, No. 9, 2000, pp. 985–1001.
doi:10.1016/S0967-0661(00)00046-0

[21] Lampton, A., and Valasek, J., "Predicition of Icing Effects on the Dynamical Response of Light Airplanes," *Journal of Guidance, Control, and Dynamics*, Vol. 30, No. 3, May–June 2007, pp. 722–732.

[22] Lampton, A., and Valasek, J., "Prediction of Icing Effects on the Lateral/Directional Stability and Control Light Airplanes," AIAA Paper 2006-6487, Aug. 2006.

[23] Advanced Aircraft Analysis Software, Design, Analysis, and Research Corporation, Lawrence, KS, 2003.

[24] Sadraey, M., and Colgren, R., "Derivations of Major Coupling Derivatives, and the State Space Formulation, of the Coupled Equations of Motion," AIAA Paper 2006-7790, Sept. 2006.

[25] Anon., "Cessna Aircraft Company Model 208 Maintenance Manual," Cessna Aircraft Company, Wichita, KS, April 1996.

[26] Lampton, A., and Valasek, J., "Prediction of Icing Effects on the Stability and Control of Light Airplanes," AIAA Paper 2005-6219, Aug. 2005.

[27] Bragg, M., and Lee, S., "Aircraft Icing Flight Dynamics Model for Twin Otter Aircraft," Rept. 10817/1329/TTM to Systems Technology, Inc., Hawthorne, CA, Oct. 2000.

[28] Roskam, J., *Airplane Design Part VI: Preliminary Calculation of Aerodynamic, Thrust and Power Characteristics*, Design, Analysis, and Research Corporation, Lawrence, KS, 1990, pp. 268–271.